

## Mars Color Imager (MARCI) on the Mars Climate Orbiter

M. C. Malin,<sup>1</sup> J. F. Bell III,<sup>2</sup> W. Calvin,<sup>3</sup> R. T. Clancy,<sup>4</sup> R. M. Haberle,<sup>5</sup>  
P. B. James,<sup>6</sup> S. W. Lee,<sup>7</sup> P. C. Thomas,<sup>2</sup> and M. A. Caplinger<sup>1</sup>

**Abstract.** The Mars Color Imager, or MARCI, experiment on the Mars Climate Orbiter (MCO) consists of two cameras with unique optics and identical focal plane assemblies (FPAs), Data Acquisition System (DAS) electronics, and power supplies. Each camera is characterized by small physical size and mass ( $\sim 6 \times 6 \times 12$  cm, including baffle;  $< 500$  g), low power requirements ( $< 2.5$  W, including power supply losses), and high science performance ( $1000 \times 1000$  pixel, low noise). The Wide Angle (WA) camera will have the capability to map Mars in five visible and two ultraviolet spectral bands at a resolution of better than 8 km/pixel under the worst case downlink data rate. Under better downlink conditions the WA will provide kilometer-scale global maps of atmospheric phenomena such as clouds, hazes, dust storms, and the polar hood. Limb observations will provide additional detail on atmospheric structure at 1/3 scale-height resolution. The Medium Angle (MA) camera is designed to study selected areas of Mars at regional scale. From 400 km altitude its  $6^\circ$  FOV, which covers  $\sim 40$  km at 40 m/pixel, will permit all locations on the planet except the poles to be accessible for image acquisitions every two mapping cycles (roughly 52 sols). Eight spectral channels between 425 and 1000 nm provide the ability to discriminate both atmospheric and surface features on the basis of composition. The primary science objectives of MARCI are to (1) observe Martian atmospheric processes at synoptic scales and mesoscales, (2) study details of the interaction of the atmosphere with the surface at a variety of scales in both space and time, and (3) examine surface features characteristic of the evolution of the Martian climate over time. MARCI will directly address two of the three high-level goals of the Mars Surveyor Program: Climate and Resources. Life, the third goal, will be addressed indirectly through the environmental factors associated with the other two goals.

### 1. Introduction

In May 1995 the National Aeronautics and Space Administration (NASA) announced the opportunity to participate in a mission to conduct observations of Mars from a circular, polar, 400 km altitude orbit. The primary goal of the Mars Surveyor 1998 Orbiter was to recover observations lost when the Mars Observer mission failed in 1993, by re-flying one of two Mars Observer experiments. Shortly after the announcement, NASA chose the Pressure Modulator Infrared Radiometer (PMIRR) as the primary payload and focused the 1998 mission on collecting measurements of climatologically important atmospheric parameters (atmospheric pressure and temperature, water abundance, and dust loading) over a Martian year. NASA's original announcement specifically called for proposals to build and operate, as a secondary experiment, a small imaging system to complement PMIRR within extreme re-

source constraints. In particular, only \$3 million and 3 kg were allocated to the imaging experiment.

The Mars Color Imager, or MARCI, consists of two cameras with unique optics and identical focal plane assemblies (FPAs), Data Acquisition System (DAS) electronics, and power supplies. Each camera is characterized by small physical size and mass ( $\sim 6 \times 6 \times 12$  cm, including baffle;  $< 500$  gm), low power requirements ( $< 2.5$  W, including power supply losses), and high science performance ( $1000 \times 1000$  pixel, low noise); see Table 1.

The Wide Angle (WA) camera is capable of mapping Mars in five visible and two ultraviolet spectral bands at resolutions from a kilometer to 12 km per pixel, depending on downlink data rate and pixel summing. Under typical downlink conditions the WA will provide kilometer-scale global maps of atmospheric phenomena such as clouds, hazes, dust storms, and the polar hood. Limb observations will provide additional detail on atmospheric structure at 1/3 scale-height resolution.

The Medium Angle (MA) camera is designed to study selected areas of Mars at regional scale. Its  $6^\circ$  FOV, which covers  $\sim 40$  km at 40 m/pixel from the 400 km nominal orbit altitude, will permit all locations on the planet except the poles to be accessible for image acquisitions roughly once every 2 months. Eight spectral channels between 425 and 1000 nm provide the ability to discriminate both atmospheric and surface features on the basis of composition.

In the following sections we describe the science objectives and goals of the MARCI investigation. We then provide a technical description of the instrument, and conclude with a discussion of the operational constraints imposed by Mars Sur-

<sup>1</sup>Malin Space Science Systems, San Diego, California.

<sup>2</sup>Center for Radiophysics and Space Research, Cornell University, Ithaca, New York.

<sup>3</sup>U.S. Geological Survey, Flagstaff, Arizona.

<sup>4</sup>Space Science Institute, Boulder, Colorado.

<sup>5</sup>NASA Ames Research Center, Space Sciences Division, Moffett Field, California.

<sup>6</sup>Department of Astronomy, University of Toledo, Toledo, Ohio.

<sup>7</sup>Laboratory for Atmospheric and Space Physics, University of Colorado, Boulder, Colorado.

Copyright 2001 by the American Geophysical Union.

Paper number 1999JE001145.

0148-0227/01/1999JE001145\$09.00

**Table 1.** MARCI Instrument Parameters<sup>a</sup>

	Wide Angle (Global Color)	Medium Angle (Medium Resolution)
Mass and Volume		
Optics	177 g (including baffle) 4.8 × 4.8 × 3.8 cm with 4.8 × 8.6 × 1.4 cm baffle	160 g (including baffle) 5.4 × 5.4 × 5.5 cm with 5.4 × 5.4 × 1.4 cm baffle
FPA	150 g, 4.6 × 5 × ~3 cm	150 g, 4.6 × 5 × ~3 cm
DAS	100 g, 4.6 × 5 × ~1.7 cm	100 g, 4.6 × 5 × ~1.7 cm
Power supply	120 g, 3.5 × 5 × 1.3 cm (4.6 × 5 × 1.3 assembled)	120 g, 3.5 × 5 × 1.3 cm (4.6 × 5 × 1.3 assembled)
Total	527 g 5 × 8.6 × 11.2 cm (max)	510 g 5.4 × 5.4 × 12.9 cm (max)
Power	3 W imaging, <2 W standby	3 W imaging, <2 W standby
Optics	two five-element refractive lenses with dichroic beamsplitter	catadioptric lens with two spherical mirrors and six refractive elements
FOV	140° (limb to limb at 400 km altitude)	6° (42 km at 400 km altitude)
IFOV	2.4 mrad 0.96 km (nadir), 4.1 km (limb) at 400 km altitude	102 μrad 41 m (nadir) at 400 km altitude
<i>f</i> /ratio	<i>f</i> /6	<i>f</i> /2
Focal length	4.3 mm	87.9 mm
Detector	Kodak KAI-1001: 1024 × 1024 (1018 × 1008 photoactive), 9 μm pixels, 20% fill factor, interline transfer electronic shuttering	Kodak KAI-1001: 1024 × 1024 (1018 × 1008 photoactive), 9 μm pixels, 20% fill factor, interline transfer electronic shuttering
Noise	30 e <sup>-</sup>	30 e <sup>-</sup>
Full-well	>30,000 e <sup>-</sup>	>30,000 e <sup>-</sup>
Digitization	8-bit flash ADC with charge-domain square-root encoding	8-bit flash ADC with charge-domain square-root encoding
Exposure time	0.25 s	12.1 ms
Band pass	7 bands, 50 nm width bandcenters: 280, 315, 453, 561, 614, 636, 765 nm	8 bands, 50 nm width bandcenters: 445, 501, 562, 639, 767, 829, 903, 1002 nm

<sup>a</sup>MARCI, Mars Surveyor 1998 Orbiter Color Imager.

veyor 1998 Orbiter (now called the Mars Climate Orbiter, or MCO) mission design.

## 2. Science Objectives and Goals

MARCI is primarily an atmospheric experiment. Its daily, global, kilometer-scale maps of atmospheric phenomena will be used directly to study Martian meteorology. In addition to tracking atmospheric phenomena in space and time, the MARCI investigation will use ozone as a surrogate for water vapor and cloud motions as a surrogate for wind measurements to study the present global circulation. Wind streaks, polar deposits, and other wind-shaped or modified landforms will be used to study past circulation relationships.

MARCI is secondarily a geological experiment. Chemical and mineralogical composition remain major gaps in understanding Mars; the Mars Global Surveyor (MGS) Thermal Emission Spectrometer (TES) is currently addressing these gaps, and the 2001 flight of the gamma ray spectrometer (GRS) and a thermal emission imaging system (THEMIS) will provide additional data. MARCI will contribute to compositional studies primarily through measurement of reflectance properties dominated by weathering products. Observations at several spectral wavelengths will permit discrimination of the composition of adjacent surface materials. The higher spatial resolution that MARCI affords at the expense of spectral detail complements the lower spatial, higher spectral resolution of TES. Diurnal coverage by the WA and bimonthly coverage by the MA permit searches for changes that reflect both climate and material. While not an imaging spectrometer, MARCI will be able to discriminate between many important weathering products derived from the volcanic rocks that clearly dominate the surface of Mars.

MARCI is synergistic with the PMIRR experiment on the Mars Climate Orbiter. The UV and visible dust and cloud opacities retrieved from MARCI limb observations, when combined with the PMIRR thermal IR dust and cloud opacities, will yield a unique definition of the full radiative properties of Mars dust and cloud aerosols. Current uncertainties in the solar absorption and IR cooling properties of the dust are sufficiently large that net cooling or heating of the lower Mars atmosphere [Haberle and Jakosky, 1991; Clancy *et al.*, 1995] cannot be discriminated. Combined visible and IR cloud opacity measurements (which do not at present exist) would allow critical definitions of the cloud particle sizes [Clancy and Lee, 1991]. These dust and cloud particle measurements could be studied as a function of altitude and season from joint MARCI and PMIRR observations.

Although the MARCI ozone observations are sufficient alone to infer atmospheric water variations, they will provide a much stronger investigation of Mars atmospheric photochemistry when combined with direct water vapor measurements made by PMIRR. Current photochemical modeling is limited by the lack of simultaneous ozone and water profile measurements [e.g., Nair *et al.*, 1994]. The ability to measure both with detailed seasonal, vertical, and latitudinal information will provide, by far, the strongest observational constraints to date on Mars photochemistry.

Like PMIRR, MARCI is both a nadir and limb viewing instrument. The visible and UV limb profiles derived from MARCI data will complement the IR profiles extracted by PMIRR. The spatial resolution at the limb of the two data sets is roughly comparable (~1/3 of a scale height), which facilitates intercomparison.

The delay in the start of the MGS mapping mission means

that MARCI operations will overlap with both Mars Orbiter Camera (MOC) and TES activities for  $\sim 1$  year. Near-coincident WA observations at two different local times will enable joint study of the diurnal dependence of clouds and weather systems. MARCI observations will support interpretation of in situ observations by the Mars Surveyor 1998 Lander (the Mars Polar Lander, or MPL). Coordinated MARCI MA and MOC Narrow Angle (NA) observations will permit MARCI surface targets to be characterized at meter scale, and MA images can provide context for NA images vastly superior to that provided by the MOC WA. Additionally, locations of specific interest already identified in panchromatic NA observations can be imaged in multiple colors and used to extend geologic contacts over larger areas.

## 2.1. Atmospheric Studies

Atmospheric investigations will include studies of (1) the distribution of dust, condensates, and ozone in the atmosphere, (2) the structure of condensate clouds and their relationship to topography and to circulation patterns predicted by global circulation models (GCMs), (3) dust storms ranging in magnitude from localized clouds to planet-encircling storms, and (4) polar phenomena. Examples of several of these phenomena are seen in the Hubble Space Telescope (HST) image in Plate 1.

The major scientific questions to be addressed are as follows:

1. What is the seasonal and geographical variability in dust, ozone, and condensates in the Martian atmosphere?
2. What is the general circulation of Mars? How reliable are the predictions of global circulation models (GCMs), and how much interannual variability exists?
3. What role do water ice clouds in the equatorial cloud band (ECB) and in the polar hoods play in the Martian water cycle, in particular in controlling the net annual transfer of water between hemispheres?
4. How do local, regional, and global dust storms evolve? How are they related to the local, mesoscale, and synoptic-scale circulations?
5. How are the seasonal and residual caps involved in the global transport of water and dust on Mars? What is the direction of the net annual water transport on the planet?

**2.1.1. Clouds.** Clouds probe many important microphysical and radiative properties of the Martian atmosphere and may be used to test dynamical atmospheric models. The horizontal and vertical distributions of ice aerosols are determined by a complex balance between cloud microphysics and large-scale transport. Global, synoptic cloud observations in nadir and limb geometries are the best way to study the geographical, vertical, and temporal distributions of Martian clouds in order to constrain circulation models. Such cloud observations also allow estimates of the impact of water vapor saturation conditions on the meridional transport of total water (ice plus vapor), in terms of long-term and seasonal behaviors of polar and atmospheric water inventories.

In addition, dust and ice aerosols in the Martian atmosphere may exhibit nonlinear radiative interactions that enhance the spatial, seasonal, and interannual variabilities of atmospheric temperatures, aerosol, and water vapor conditions [Clancy *et al.*, 1996b; A. V. Rodin *et al.*, Thermal feedback between dust and water ice clouds in the Mars atmosphere: Implications for the aphelion climate, submitted to *Icarus*, 1999]. In this case a comprehensive study of Mars cloud behavior requires correlative measurements of the vertical distributions of atmospheric

water vapor, temperatures, and the densities and particle sizes of the constituent materials of atmospheric dust and clouds. MARCI multispectral imaging of cloud and dust aerosols, in conjunction with PMIRR and TES measurements of temperature, water vapor, ice, and dust IR opacities, provides our first opportunity to conduct such a complete investigation of Martian cloud microphysics.

**2.1.2. General circulation.** The general circulation of the Martian atmosphere determines the transport of dust and water and affects the rate at which  $\text{CO}_2$  condenses at the poles [Pollack *et al.*, 1990, 1993]. Existing observations lack the spatial and temporal density needed to constrain GCMs; thus a primary goal of this investigation is to help describe the structure and variability of the general circulation.

Winds can be determined from imaging data by tracking cloud systems and dust storms and can also be inferred from topographically generated gravity wave trains whose wavelengths are diagnostic of the local wind field. Although such observations cannot describe the full three-dimensional structure of the general circulation, previous experience on Mars suggests that they can be used to follow atmospheric motion. Of particular importance is the nature of traveling baroclinic wave systems. GCMs suggest that they may be much less vigorous in the southern hemisphere during winter than in the northern hemisphere, owing to hemispheric differences in topography [Barnes *et al.*, 1993]. It is necessary to characterize the dominant zonal wave numbers, phase speeds, and meridional structure of these systems in both hemispheres if the general circulation models are to be validated. Models also predict that, at least in the northern hemisphere, baroclinic disturbances should grow and decay in preferred longitudinal regions called "storm zones" [Hollingsworth *et al.*, 1995; Barnes *et al.*, 1996]. In these regions the poleward fluxes of heat and momentum are maximized, and dust and water transport should be as well. Topography is mainly responsible for the stationary eddies and should produce interhemispheric differences in storm zone patterns. Atmospheric opacity and cloud frequency and optical properties should reveal these zones as persistently dustier and cloudier regions. Models also predict that the Martian Hadley cell is much more longitudinally variable than previously thought. In particular, the meridional flow in the lower branch of the Hadley cell should be channeled into narrow currents along the eastward flanks of major topographic rises such as Tharsis. Imaging data can be used to test this model prediction.

**2.1.3. Interannual climate variations.** Ground-based temperature profiling and HST imaging since 1988 show much colder atmospheric temperatures and lower dust loading than has been inferred from the Viking 1976–1979 period of observations [Clancy *et al.*, 1990, 2000; James *et al.*, 1994]. This distinction appears most significant for the northern spring/summer season of Mars (around Mars aphelion). The typical behavior of the Martian aphelion atmosphere may include low dust loading, reduced atmospheric temperatures, low altitudes of water vapor saturation, and a  $10^\circ\text{S}$ – $30^\circ\text{N}$  global belt of moderate opacity clouds [Clancy *et al.*, 1996a]. Clancy *et al.* argued that the increased prominence of clouds in this season may reflect important radiative instabilities associated with ice nucleation on dust aerosols, which serves to increase interannual and seasonal variations in the current Martian atmosphere.

While such radiative forcing by Martian ice clouds is not established, the presence of the global aphelion cloud belt has

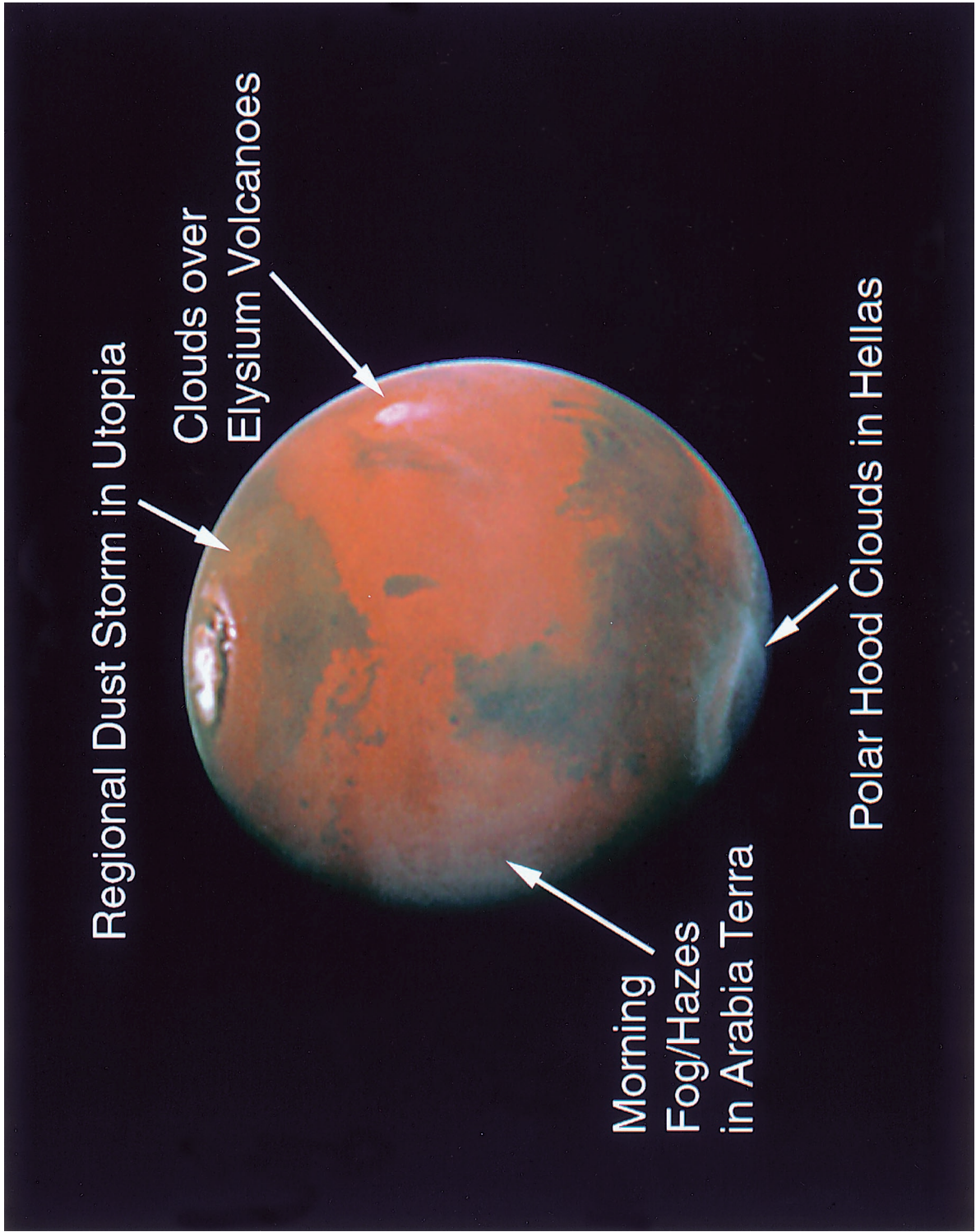


**Plate 1.** This Hubble Space Telescope (HST) image of Mars obtained in April 1995 displays a rich assortment of atmospheric phenomena.

recently been observed by MOC imaging and TES IR spectroscopic observations in 1999. MARCI cloud imaging in subsequent Mars aphelions can be compared to HST and MOC imaging of current and past Mars aphelions to determine the degree of interannual variability in this diagnostic aphelion cloud belt, both for its detailed seasonal development and for its vertical and latitudinal extents. Comparisons of the continuous mapping observations of MOC and MARCI, in particular, will define the degree of interannual variability for this global cloud belt as well as the substantial interannual variability of perihelion dust storms in unprecedented detail.

**2.1.4. Dust storms.** Global maps are important for monitoring all but the smallest-scale dust activity on Mars. Viking observations showed that local sand or dust storms are fairly common in certain locales and during certain seasons on Mars, e.g., at the edge of the South Cap in spring, in Hellas and Argyre Basins, in the Solis Planum region, etc. More recent HST [James *et al.*, 1999] and MGS observations have expanded the domain of Martian dust storms. On rare occasions during the Viking mission, single storms were monitored with sufficient temporal sampling density to determine the evolution of these events. However, major questions remain about the diurnal development of local storms, especially in the polar regions.

The expansion of global storms has been observed from Earth as well as by Viking using sequences of images [Martin, 1976], and the path of a large regional storm in the northern hemisphere was deduced from Viking sequences obtained on 3 consecutive days in 1978 [James, 1985]. Observation of Mars for 1 year at a scale of better than 10 km should be sufficient to define the global dust cycle for that year and will help to identify sources and sinks for dust. Coupled with a successful MGS MOC experiment, this would provide complete records of two consecutive seasonal dust cycles that could then be applied to addressing the circumstances that lead to planet-encircling storms and the origin of the interannual variability in the dust cycle.

There also remain significant issues regarding dust processes at smaller scales. Little is known about dust devils of the type observed by Thomas and Gierasch [1985] and, indirectly, by Ryan and Lucich [1983] using Viking Lander meteorology. Regions where local dust storm activity is known to occur, such as preferred longitudes at the edge of the receding spring caps, may also be likely sites for dust devil activity. Inspection of these areas will shed light on how local storms are started and how topography, surface, local sources of dust, and other physical factors participate in their generation.

**2.1.5. Polar processes.** The annual cycles of the polar caps are the most obvious signature of a seasonal cycle on Mars, having been recognized as such by Herschel [1784]. A good data set at better than 1 km/pixel resolution was obtained by Viking Orbiter 2 for a south cap recession [James *et al.*, 1979], while the best views of a north polar recession prior to MGS were obtained by Mariner 9 and the HST. Neither spacecraft nor Earth-based imaging has provided much information on the deposition of either cap, partly because most condensation takes place during polar night but also because of condensate polar hood clouds that confuse separation of surface and atmospheric effects. Global monitoring with the multispectral MARCI cameras should reveal the relationships between the polar hood and cap edges.

The observational situation is better for the residual polar caps. Untangling the physics of the residual caps is one of the

most intriguing problems in Mars science because of the dichotomy in composition between the water ice north cap and the (at least partially) dry ice south cap. Involved in this puzzle are clues to the water cycle on Mars; net annual transfer of water from one hemisphere to another may be revealed by interannual changes in the residual caps. Such changes were seen in a comparison of the very good Mariner 9 and Viking data sets, and data from MGS and MCO will provide additional reference points for identification of possible secular or cyclic variations with periods  $>1$  Mars year. The residual polar caps will also be studied at medium resolution in order to study the behavior of the surface and to estimate the thickness of the frost deposits.

The reflectivity of surface frost at several wavelengths and at a variety of photometric angles will be used to investigate the nature of the ice surface. Changes in the frost albedo as a function of wavelength can be compared to the atmospheric opacity to attempt to correlate changes in the frost surface with dust deposition and other seasonal and geographic variables.

In particular, spatial heterogeneity in the receding seasonal cap has been observed [e.g., James *et al.*, 1992; Calvin and Martin, 1994], yet the influence and interplay of local topography, underlying geology, and insolation variation is not well known. An unusual and as yet not well understood phenomenon is noticed in the south polar residual cap data from TES where the albedo of a particular region darkens yet the area remains cold [Kieffer *et al.*, 1998]. This area also had unusual reflectance properties when observed in MOC WA imaging [James *et al.*, 2000]. It is possible that this region may sublime overlying thin CO<sub>2</sub> frost and expose a thick layer of semitransparent CO<sub>2</sub> ice underneath. This possibility was also discussed by Calvin and Martin [1994]. MARCI, in conjunction with PMIRR, will allow us to search for more of these unusual areas in the seasonal deposits. The regions are highly localized, and their relationship to underlying geology can be determined at spatial scales much better than TES. In addition, MARCI color information may help determine the attenuation of reflected light and estimate to first order the thickness of such deposits.

## 2.2. Dust, Cloud, and Ozone Opacities

Aerosol and ozone opacities will be retrieved from MARCI multispectral nadir and limb imaging. MARCI wide-angle images will provide accurate horizontal and vertical mapping of Martian atmospheric opacity structures. The multispectral character of the MARCI images will allow separation of dust and ice aerosols, and the ultraviolet (UV) MARCI channels will provide unique determinations of ozone opacity. The use of combined visible/ultraviolet imaging of Mars has been demonstrated by HST observations to provide strong constraints on dust, cloud, and ozone opacities in the Mars atmosphere [James *et al.*, 1994; Clancy *et al.*, 1999; Wolff *et al.*, 1999]. The key strengths of the 230–330 nm observations are the low albedos of the Mars surface (0.01–0.02 [Hord *et al.*, 1974]) relative to atmospheric Rayleigh scattering, the resulting sensitivities to small dust and cloud opacities ( $<0.05$ ; see below) in nadir as well as limb viewing, and the ability to observe the Hartley band absorption of atmospheric ozone as a proxy for Mars atmospheric water vapor [Barth *et al.*, 1973; James *et al.*, 1994]. The combination of MARCI visible and UV limb imaging discriminates dust from cloud aerosols and provides vertical profiling of cloud, dust, and ozone opacities over altitudes of 0–50 km. Each of these capabilities is described below in

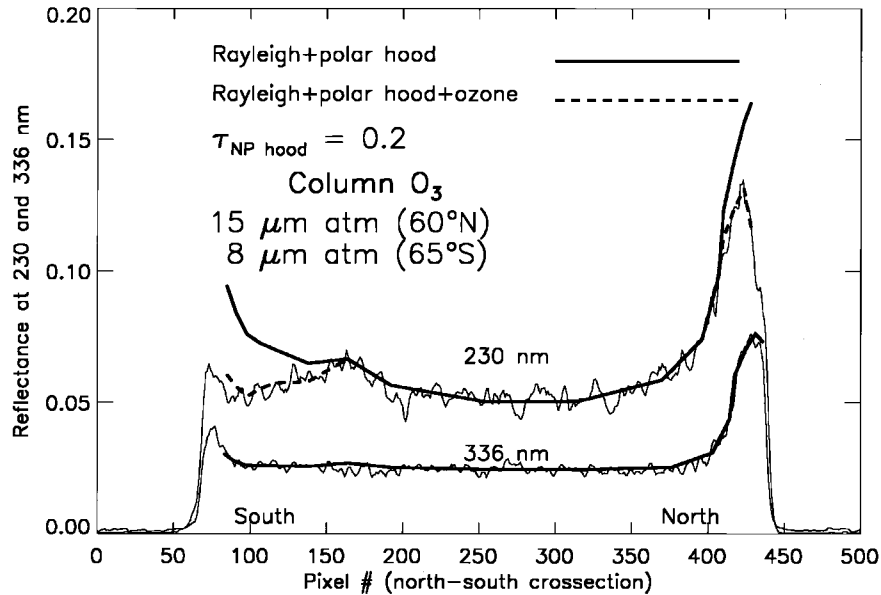


**Figure 1.** UV reflectance and column density of  $O_3$  from HST observations from December 13, 1990 ( $L_S = 348^\circ$ ,  $D_{Mars} = 16.5''$ ). The dashed line curve of 230 nm brightness models the effect of Hartley band ozone absorption on the observed 230 nm brightness.

terms of specific measurement/retrieval goals and methods for the MARCI experiment.

**2.2.1. Cloud opacities.** Clouds appear very bright against the dark surface of Mars at violet and UV wavelengths. Figure 1 presents north-south cross sections of 230 and 336 nm brightnesses from December 1990 HST images of Mars [from James *et al.*, 1994], in which the north polar hood ( $\tau \sim 0.2$ ) appears roughly 3 times brighter than the surface plus Rayleigh atmospheric reflectances. Also, note the violet image projection of the low-latitude cloud belt observed around Mars aphelion by HST in 1995 [James *et al.*, 1994] and 1997 (Figure 2). Neither of these large-scale cloud systems is very apparent in green and red light imaging, and the spatial variations of such diffuse

clouds are not easily separated from the strong spatial variations of surface albedos at these longer wavelengths. The very low surface albedos in the UV and the distinct Rayleigh scattering component of the UV reflectance (note the presence of the enhanced Rayleigh scattering over Hellas Basin, pixels 125–175 in the 230 nm cross section of Figure 1) provide optimum mapping of cloud opacities as small as 0.02, from nadir viewing. In limb-viewing geometry, MARCI should obtain the vertical distribution of clouds with  $\sim 4$  km vertical resolution to altitudes as high as 70 km, depending on the cloud optical depths and vertical distributions. The combined UV/visible imaging will also distinguish dust and cloud aerosol scattering, as described below.

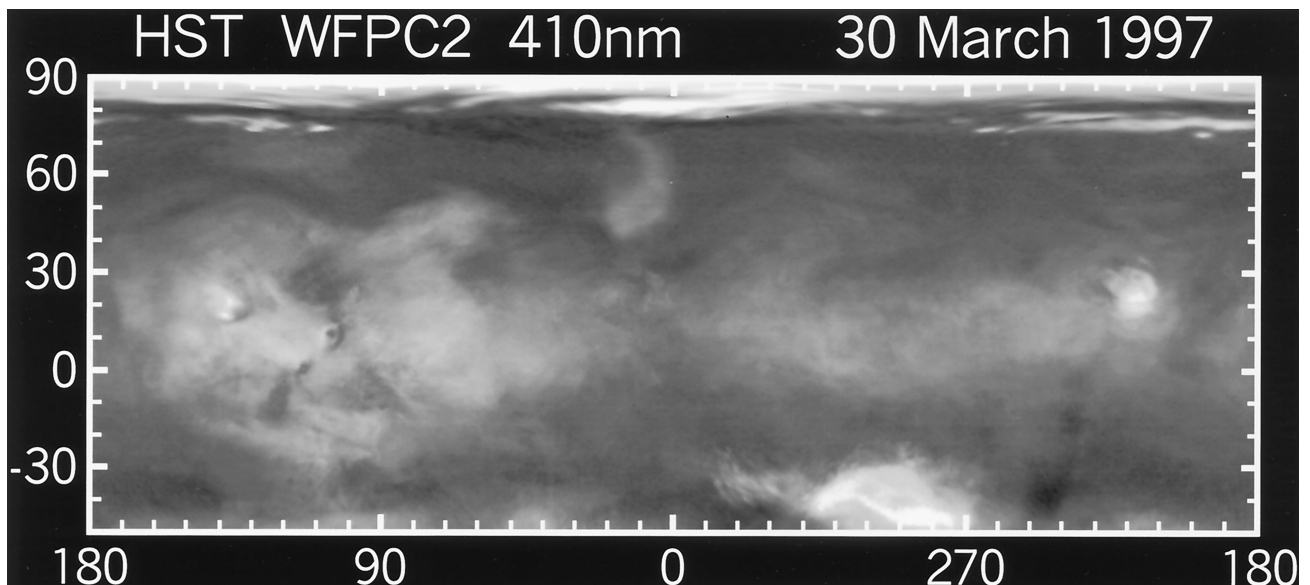


**Figure 2.** HST image of Mars at 410 nm showing the equatorial cloud band that was observed in 1995 and 1997.

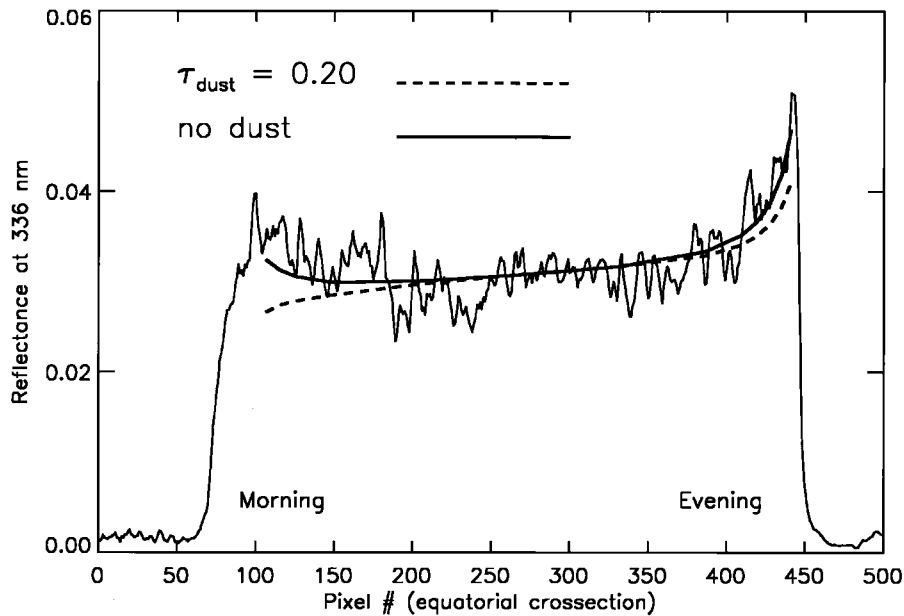


**Figure 3.** The 336 nm limb radiance of the Mars atmosphere observed by HST on December 13, 1990 ( $L_S = 344$ ,  $D_{\text{Mars}} = 16.5''$ ) shows the effects of dust at the limb of Mars, where the optical columns of molecular scattering and dust absorption are enhanced.

**2.2.2. Dust opacities.** Owing to the low single-scattering albedo of the dust particles in the UV ( $\sim 0.4\text{--}0.6$  [Pang and Ajello, 1977]) and the substantial UV Rayleigh scattering optical depths of a 6 mbar  $\text{CO}_2$  atmosphere ( $\tau_{\text{nadir}} = 0.03$  at 336 nm), dust loading leads to significant decreases in the UV brightness of the Mars atmosphere. This effect is most strongly exhibited on the atmospheric limb of Mars, where the optical columns of molecular scattering and dust absorption are enhanced. Figure 3 shows an equatorial cross section of the observed 336 nm limb radiance of the Mars atmosphere as observed by HST on December 13, 1990 [from James *et al.*, 1994]. Multiple scattering radiative transfer calculations are presented for two cases incorporating simple surface and atmospheric molecular scattering (solid line) and surface and atmospheric molecular scattering with a dust opacity of 0.2 (dashed line). Note that ozone absorption is not present at 336 nm (see below). These model calculations extend only to emission angles of  $65^\circ$  and have been normalized to the observed radiances at the Mars disk center to reflect the uncertain calibration of the WF/PC I UV imaging [James *et al.*, 1994]. At visible wavelengths, dust appears as distinct atmospheric limb brightening rather than absorption, because the dust single-scattering albedo is high ( $\sim 0.9$ ) and Rayleigh scattering is minuscule [e.g., Clancy and Lee, 1991]. As a consequence, strong discriminations of dust versus cloud aerosols are provided from the combined visible/UV limb observations. Given the spatial resolution of the MARCI limb measurements ( $\sim 4$  km versus  $\sim 50$  km for the HST images), sensitivities to minimum dust column opacities of 0.05, as well as the 0–50 km profile of dust opacity during high dust loading ( $\tau > 1$ , with  $\sim 10$  km vertical resolution) should be obtained. However, dust loading in the lower 10 km of the atmosphere must be derived at non-limb-tangent viewing owing to the greater than unity dust/Rayleigh limb optical depths for the lower scale height.

**2.2.3. Ozone opacities.** High-latitude determinations of ozone columns are presented in Figure 1, where the dashed

line curve of 230 nm brightness models the effect of Hartley band ozone absorption on the observed 230 nm brightnesses. MARCI will use a wavelength of 250 nm, which is more optimally placed within the Hartley ozone band. Since ozone absorption is negligible at 330 nm, the determination of Mars atmospheric ozone opacities will be obtained from the ratio of the observed 250 and 330 nm radiances. The observed air mass dependence of the 250 to 330 nm brightness ratio leads to a determination of the ozone opacity that is fairly insensitive to calibration and modeling uncertainties. The variation of this ratio on the atmospheric limb provides for about one scale height (10 km) resolved profiles of the ozone absorption over the 0–40 km altitude range, although ozone retrievals in the lowest scale height must rely on viewing air masses below the limb tangent (path lengths of 2–4). MARCI will have the sensitivity to measure ozone columns of  $1 \mu\text{m atm}$ , sufficient to observe the smaller ozone abundances at low latitudes ( $\sim 2 \mu\text{m atm}$  [Espanak *et al.*, 1991]) as well as the larger high-latitude ozone levels shown in Figure 1. Mars atmospheric ozone is photochemically tied to atmospheric water vapor, such that it varies inversely with atmospheric water [e.g., Nair *et al.*, 1994]. Hence the observed variations of ozone provide key information on the seasonal and spatial variations of Mars atmospheric water. Furthermore, recent observations of low-altitude water vapor saturation around Mars aphelion [Clancy *et al.*, 1996a] have been correlated with large increases in atmospheric ozone, from HST 1995 Faint Object Spectrograph observations [Clancy *et al.*, 1996b, 1999]. These key aphelion changes in Mars ozone behavior can be measured in much greater detail by MARCI.

### 2.3. Surface-Atmosphere Interactions

Given the current lack of fluvial activity on Mars, processes involving surface-atmosphere interactions (SAI) are the primary agents of surface change at present. Manifestations of SAI include regional and global-scale dust storm activity, ubiq-

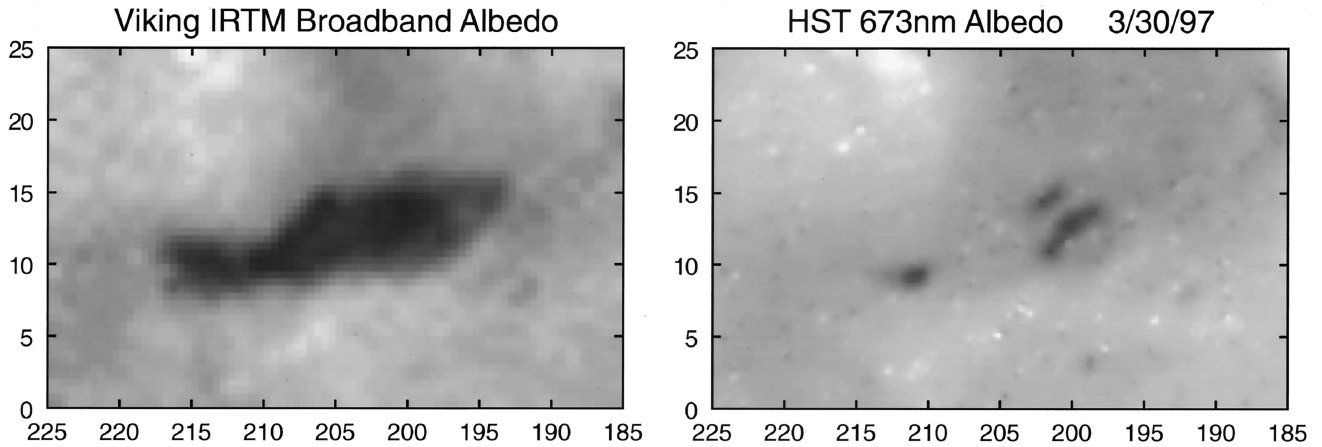


**Figure 4.** Observations of changes in a major albedo feature on Mars (Cerberus) are revealed in this comparison of Viking infrared thermal mapper and HST 673 nm maps of the area.

uitous wind-related features such as sand dunes, the variability of surface albedo features related to aeolian transport of dust and sand, and the condensation/sublimation of volatiles at the surface. The accumulated historical evidence (ground-based, spacecraft, and HST observations) indicates that a great deal of seasonal and interannual variability exists in aeolian activity on Mars. For example, previous observations have revealed a great deal of interannual variability in the timing, location, and extent of dust storms, the primary source of short-term changes in the appearance of Mars at present [Slipher, 1962; Zurek, 1982; Martin, 1984; Peterfreund, 1985]. Acquisition of data for more than 1 Martian year will significantly expand the temporal observations that are crucial to understanding the seasonal, interannual, and long-term SAI.

### 2.3.1. Variable features resulting from dust transport.

There is abundant evidence that, at present, aeolian processes are active over most of the surface of Mars [cf. Veverka *et al.*, 1977; Thomas *et al.*, 1981]. A wide variety of surface features, such as wind streaks, sand dunes, and regional albedo features, are attributed to aeolian deposition and erosion. Previous studies have demonstrated that variations in regional albedo and wind streak patterns are indicative of sediment transport through a region [Lee *et al.*, 1982, 1994; Kahn *et al.*, 1992], while thermal inertia data (derived from Viking infrared thermal mapper (IRTM) observations and to be derived at high spatial resolution from MGS TES measurements) are indicative of the degree of surface mantling by dust deposits [Kieffer *et al.*, 1977; Christensen, 1982, 1986a, b, 1988; Jakosky, 1986]. An example is the change in the Cerberus region from the time of Viking observations as recently viewed by HST and shown in Figure 4. Experimental studies [Wells *et al.*, 1984] show that small amounts of dust deposited/eroded from the surface can explain the observed surface albedo changes (modifying surface dust cover by less than a micron of dust can alter the albedo by several tens of percent). The colors of Martian albedo features can also be related to variable amounts of dust cover [Soderblom *et al.*, 1978; Singer and McCord, 1979; McCord *et al.*, 1982a, b]. Visual data are therefore diagnostic of net erosion or deposition of dust-storm fallout that is taking place currently; when they are combined with available thermal data, inferences can be made as to whether such processes have been active in a region over the long term. In addition, there is evidence in MGS MOC images that some features previously

believed to be primarily related to dust transport may in fact result from both dust and sand transport (see following section).

While the basic distribution, season of formation, effective wind directions, and perhaps meteorological conditions involved in the formation of variable features have been documented with previous observations, the actual conditions of dust entrainment and deposition related to these features have remained elusive. The orbit and payload of MCO is particularly well suited to provide the detailed temporal, spatial, and multiwavelength studies needed to significantly advance our understanding of these processes; the scientific yield will be further enhanced by coupling with observations of atmospheric dust loading to be made by PMIRR. Regularly repeated global mapping by the MARCI WA is ideal for monitoring regional albedo features and for detecting areas undergoing albedo variations. Observations by MA can then be targeted for detailed examination of currently active variable features. Such observations are pertinent at a variety of scales, allowing comparisons to general circulation models (global-scale wind patterns) as well as investigation of individual features (local winds [cf. Magalhaes and Young, 1995]).

### 2.3.2. Variable features resulting from sand transport.

Sand dunes are markers of a specific physical process (saltation) and hence are powerful indicators of both short-term and accumulated surface wind stress. Their widespread, but not ubiquitous, distribution on Mars allows a wide sampling of aeolian transport conditions [Thomas and Weitz, 1989; Thomas and Gierasch, 1995; Greeley *et al.*, 1992]. Multispectral observations by the MARCI MA can address several key questions related to Martian dunes, such as interannual variability (based on comparisons with Mariner 9, Viking, and MGS observations of specific dune fields), components of dunes and their relationship to sediments in the source deposits, detailed morphology of dune fields, and the relationship to local, regional, and global atmospheric circulation (i.e., using dunes as wind, paleowind, and climate indicators).

MGS MOC images indicate that some variable features may involve both sand and dust: albedo features that were seen over 20 years ago are delineated by accumulations (possibly sand) in low areas of rough volcanic terrain. The wind streaks may vary by addition and removal of dust, but the locus may in part, or in full, be determined by where the sand transport

system has left low areas (a few meters scale roughness) filled. The color capabilities of MARCI will allow considerable refinement of what these materials (seen only in broadband "clear" MOC images) are and how the sand and dust transport are related. MOC has also seen a variety of dune albedos [Thomas *et al.*, 1999]; many of these are large enough to be mapped by MARCI. In particular, correlation of these dune colors with nearby outcropping materials may establish length of transport of different materials.

#### 2.4. Surface Studies: Morphology and Pattern

MARCI permits imaging studies of surface features and processes that were not possible with the Viking Orbiter or MGS cameras. Of most interest to surface studies is the ability to acquire moderate resolution data through multiple filters over sufficient area to provide both morphologic and surface unit information.

**2.4.1. Aeolian sediments and morphology.** Aeolian deposits on Mars range from micron-thick dust coatings to multikilometer thick polar deposits. Aeolian transport has been important in moving material for much of Mars' history, and the transport has been global in scale. In the previous sections, aeolian materials were discussed as measures of past and present atmospheric phenomena and tracers of surface-atmosphere interactions. Here they are considered in their own right, as deposition and erosion of aeolian materials are geologic processes as well, and provide great insight into the geological history of Mars. Deciphering the materials and stratigraphy of the wide variety of aeolian deposits on Mars is crucial to understanding the geological influences of climate on Mars and the relationship of current processes to past ones. Appropriately selected pixel scales, image formats, and spectral wavelengths will allow investigation of aeolian materials and stratigraphy not possible with previous Mars missions, including MGS.

**2.4.2. Polar deposits.** The polar deposits, thought to be climatically sensitive because of their association with frost deposition, include at least two nonvolatile components as indicated by Viking Orbiter color data [Herkenhoff and Murray, 1990; Thomas and Weitz, 1989]. The layered deposits appear to reflect cycles of deposition and erosion on a variety of time-scales, and their overall extent has been reduced from previously larger deposits [Thomas *et al.*, 1992]. The makeup of the layers, the relationship of unconformities to the various layers and other sedimentary units, and the erosional forms at several scales around the deposits will be incompletely explored before MCO. Coverage of selected areas of the layered deposits, chasmata, deposits marginal to the layered deposits, and polar dunes with four or five filters between 450 and 900 nm can provide far more discrimination of surface units than was possible using Viking images. Even with two broadband filters centered at 450 and 590 nm, Viking was able to discriminate several stages of mixing of at least three end-members in many regions of Mars. With filters giving some discrimination between 800 and 900 nm (where iron oxidation state greatly varies reflectances), it is possible to anticipate at least an order of magnitude improvement in spectrally mapping exposed units, which the Viking, and even HST, data [Bell *et al.*, 1995] suggest are present in considerable complexity and discernible because of patchiness in dust coverings. Spatial resolution of tens of meters permits local morphology to be associated with color units. This is particularly useful in relating materials exposed on dunes and wind streaks to current wind regimes

and relating morphologies to source areas as can be done in terrestrial dune fields that have multiple sources [Blount *et al.*, 1990]. The primary questions to be addressed include the following: How many different materials make up the polar deposits, and on what scales are they segregated? Are the layers distinct materials or distinct surface textures? Are the peripheral sediments sources of, or derived from, the polar layered deposits? How do the sediment transport patterns shown by older deposits compare to present-day winds? Is there a correlation of size of features (reconstitution time?) and orientation?

**2.4.3. Midlatitude and low-latitude deposits.** Transport of dust and sand at midlatitudes and low latitudes is presently dominated by Hadley circulation in southern summer [Greeley *et al.*, 1993; Thomas and Gierasch, 1995]. Many dune deposits, wind streaks, and other deposits of likely aeolian (or possibly lacustrine) origin occur in these latitudes. As with polar deposits, the number of materials involved and their scales of interlayering are unknown. A primary goal of any study of such deposits is the search for indications of relict forms with local or global asymmetry different from that of the present dominant flow. Such asymmetry may be expected because the present winds are very hemispherically asymmetric and are expected to switch with the 51,000 year cycle of perihelion precession. Multicolor observations at moderate to high resolution are needed to map the morphologies and color units in key areas identified from earlier Viking Orbiter images. Study of midlatitude to low-latitude deposits is required at all scales that may reflect regional transport of materials or that may improve knowledge of the aeolian transport regime on Mars. The significance of these older deposits is necessarily closely tied to present-day variable features.

**2.4.4. Nonaeolian morphology.** Although present material transport on Mars is dominated by wind, the surface shows effects of volcanic eruptions of lavas and pyroclasts, standing and flowing water, faulting, mass wasting, thermokarst, and possibly glacial action. At large scale the morphology of Mars' surface is dominated by volcanoes, canyons, channels, and impact craters, not aeolian deposits. The global distribution, context, and general morphology of the nonaeolian forms has been well established by Mariner 9 and Viking and will be examined in extremely limited locations at very high resolution by MGS. There remains, however, a gap in resolution coverage, as the global/regional resolution Viking data are not generally much better than MGS wide angle observations (hundreds of meters). Regional mapping at tens of meters resolution over sufficient areas to supply context for individual forms will constrain the origins of many landforms for which present interpretations range from glacial to structural. As with the aeolian studies, multicolor images will be important for discriminating differences in units in which these landforms have developed.

#### 2.5. Surface Studies: Composition and Mineralogy

The measurement of normal albedo and relative reflectivity spectra of areas on Mars can provide qualitative and sometimes quantitative information on the composition, mineralogy, and relative maturity of the terrain. The materials that control the reflectivity of the Martian surface are primarily Fe-bearing minerals in various oxidation and hydration states. Therefore spectrophotometry in the near-UV, visible, and near-IR can give compositional information complementary to the mineralogical and petrological observations to be made by MGS TES.

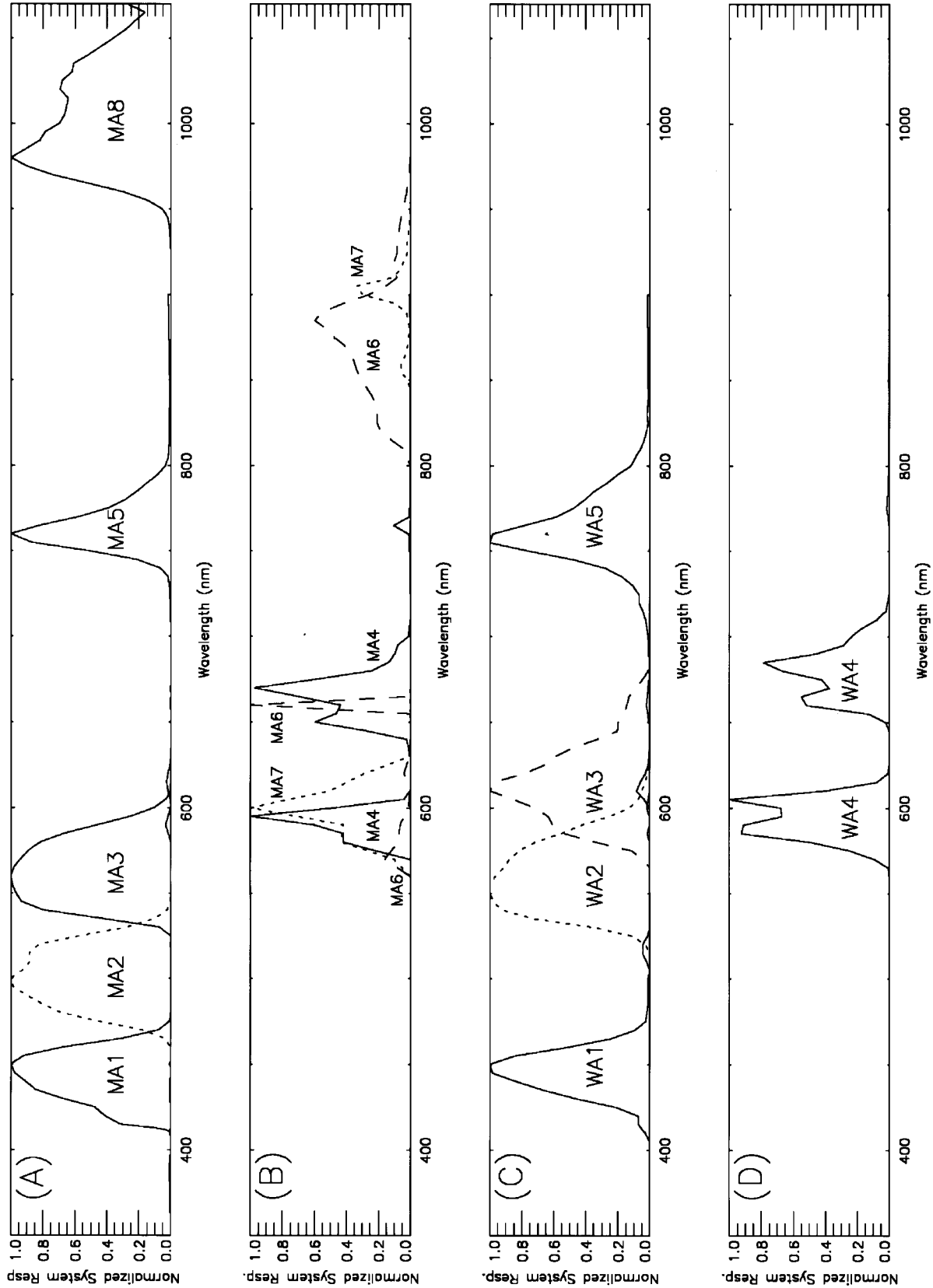


**Figure 5.** Normalized system response functions for (a) the best MARCI Medium Angle (MA) camera filters, (b) the three MA filters exhibiting poor out-of-band rejection performance, (c) the best Wide Angle (WA) camera filters, (d) the one WA filter exhibiting poor out-of-band rejection performance, and (e) the WA UV filters. Filter parameters are listed in Table 2.

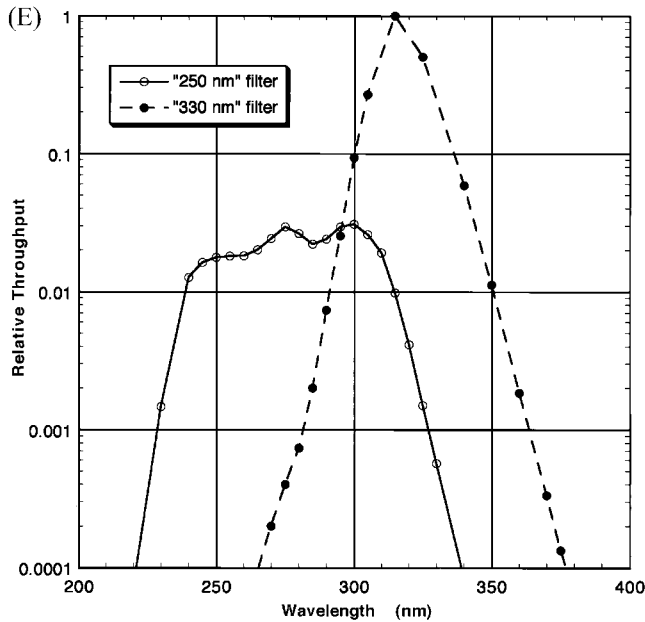


Figure 5. (continued).

The reflectance spectrum of Mars in most areas increases monotonically with wavelength, with more or less the same shape, throughout the visible portion of the spectrum. To first order, the spectra of bright areas and dark areas are remarkably similar, varying in magnitude but not relative shape. Such spectra differ, however, in the details, with broad absorption bands of low contrast (in general, these absorptions have relative magnitudes measured in the few percent). It is these differences that permit different materials to be discriminated. Only a few absorption bands are distinguishable in the visible spectrum of Mars; a few filters are sufficient to delineate their

Table 2. MARCI Multispectral Filter Characteristics

Filter	Medium Angle		Wide Angle	
	$\lambda_{\text{eff}}$ , <sup>a</sup> nm	FWHM, nm	Filter	$\lambda_{\text{eff}}$ , nm
MA1	445	51	UV1	280
MA2	501	39	UV2	315
MA3	562	50	WA1	453
MA4	639 <sup>b</sup>	107	WA2	561
MA5	767	56	WA3	614
MA6	829	50 <sup>c</sup>	WA4	636 <sup>b</sup>
MA7	903 (600) <sup>d</sup>	14 (31) <sup>d</sup>	WA5	765
MA8	1002	97		

<sup>a</sup> $\lambda_{\text{eff}}$  is the effective center wavelength of the filter, defined according to Stock and Williams [1992].

<sup>b</sup>Both MA4 and WA4 are “bimodal” filters with two response peaks from 570 to 620 nm and 650 to 720 nm (see Figure 5), so the effective center wavelength and full width at half maximum (FWHM) are technically not appropriate parameters to define these filters.

<sup>c</sup>The 829 nm filter is asymmetric and has a very narrow leak near 660 nm (see Figure 5).

<sup>d</sup>The 900 nm filter displays three transmission bands: the largest, located at 600 nm, has a FWHM of 31 nm; the second largest (63% of the largest) is centered at 903 and has a FWHM of 14 nm; and the smallest (16% of the largest) is centered at 858 nm with a FWHM of 17 nm.

positions. Thus it is possible to distinguish spectral differences regardless of the specific or quantitative compositional interpretation attached to these spectral features.

It is important to note that it is not the primary objective of this imaging experiment to provide a detailed understanding of the composition of the surface of Mars. Rather, it is the intent here to acquire multispectral (or multicolor) observations to complement the MGS TES observations in the thermal infrared with higher spatial resolution “unit” maps. These maps reflect the mineralogical composition but are more or less independent of the ability to deduce percentages of specific minerals at high spatial resolution from specific absorption features or sets of features. Observations from 400 to 1000 nm are generally sensitive to variations in the crystallinity and oxidation state of iron-bearing minerals and as such will represent primarily the distribution of weathering products and secondarily the occurrence of bedrock. MARCI will be able to provide an independent assessment of the extent to which subpixel mixing must be considered in the interpretation of observed TES spectra.

The Martian regolith can be considered to consist of three types of materials [e.g., Singer *et al.*, 1979; Soderblom, 1992]: (1) crystalline rock fragments, at a variety of sizes, consisting of basaltic materials rich in clinopyroxenes and orthopyroxenes (ferro-augite, pigeonite, etc.; enstatite, hypersthene, etc.) [e.g., Singer *et al.*, 1979; Bell *et al.*, 1990; Mustard *et al.*, 1993; McSween *et al.*, 1999] and probably other Fe-bearing minerals, including clay silicates and perhaps olivine in accessory amounts [Bell *et al.*, 1993, 2000; Geissler *et al.*, 1993; Mustard and Sunshine, 1995]; (2) weathering products, in particular, ferric oxides/oxyhydroxides such as goethite and hematite [e.g., Morris *et al.*, 1989, 2000; Bell *et al.*, 1990, 2000]; and (3) as yet poorly characterized salts and other nonsilicate minerals of undetermined origin, composition, and abundance [e.g., Clark *et al.*, 1982; Soderblom, 1992].

Spectra of the Martian surface can be interpreted primarily in terms of absorption by Fe in various mineralogic forms. Three zones of absorption-related features are superimposed on the shape of the curve in the visible and near-infrared: on the blue end (400–600 nm) is the edge of near-UV Fe<sup>3+</sup> electronic transitions and O<sup>2-</sup> → Fe<sup>3+</sup> charge transfers within Fe oxides and oxyhydroxides, which gives these minerals their distinctive reddish colors; in the center are two absorptions near 600–700 nm and 800–950 nm with band centers indicative of specific Fe<sup>3+</sup> electronic transitions in ferric oxides/oxyhydroxides; and at the red end (at and beyond 900 nm) is the famous “1  $\mu\text{m}$ ” Fe<sup>2+</sup> absorption found in many primary Fe-bearing silicate minerals [e.g., Adams, 1974; Morris *et al.*, 1985]. Because these primary and secondary minerals are related through environmentally specific physical and chemical weathering processes [e.g., Cornell and Schwertmann, 1996; Bell *et al.*, 2000; McSween *et al.*, 1999; Morris *et al.*, 2000], characterization of the Martian surface with respect to these broad compositional types, at tens of meters resolution, would greatly contribute to the understanding of Martian geologic, climatic, and weathering history.

The MARCI multispectral filter set was designed to maximize the detectability and discriminability of these different primary and secondary Fe-bearing minerals. Table 2 provides a summary of the properties of these narrowband filters, and Figure 5 shows their transmission behavior (including system response) over the spectral range of the CCDs. The MA camera has eight multispectral filters with effective central wave-

lengths ( $\lambda_{\text{eff}}$ ) from 445 to 1002 nm. The Wide Angle (WA) camera has five multispectral filters with effective central wavelengths ( $\lambda_{\text{eff}}$ ) from 453 to 765 nm. Three of the MA filters (MA4, MA6, and MA7) and one of the WA filters (WA4) were provided by the manufacturer with substantial out-of-band leaks; see Figure 5b. The usefulness and level of uncertainty of these filters in our multispectral studies are partially assessed below and are also the subject of an ongoing investigation that will be reported in a subsequent publication.

The best MA and WA filters provide enough spectral coverage and sampling to adequately assess the Fe mineralogy of regions on Mars imaged by MARCI. To demonstrate this, we analyzed a group of laboratory-measured spectra of iron-bearing minerals that have either been previously detected on Mars or could be reasonably expected to exist on the basis of available remote sensing and in situ compositional and other data. We also analyzed telescopic reflectance spectra of typical Martian bright and dark regions. Our aim was to simulate what the spectra of these materials would look like if they were observed on Mars by MARCI using both the MA and WA filter sets. We used a process similar to that of *Ockert-Bell et al.* [1997, equation (5)]. We multiplied the reflectance of each material by the solar spectral irradiance to simulate the irradiance that will actually be incident on MARCI from Martian orbit, and then we convolved this incident irradiance over the system throughput functions of each of the MARCI filters (Figure 5). This integrated irradiance was then divided by the integral of just the solar irradiance convolved over the system throughput for each filter in order to derive a simulated radiance factor ( $I/F$ ). The simulated  $I/F$  could then be compared with the original input laboratory reflectance spectrum to see how well MARCI preserves the actual spectral shapes of potential Mars surface materials.

The results of our simulation for pure mineral samples are shown in Figure 6 for both the MA and WA cameras. In general, the agreement between the high-resolution laboratory spectrum and the simulated MARCI  $I/F$  data is excellent. Filter MA7 provides essentially the same data as MA4 and is not plotted in Figure 6. The most problematic wavelengths are MA4, MA6, and WA4, which suffer to varying degrees from poor out-of-band rejection performance. In the case of MA4 and WA4, the major out-of-band leak is close enough to the intended effective center wavelength that the effect is not debilitating. Similarly, the very narrow width of the out-of-band leak in MA6 does not appear to substantially influence this filter's performance. Even without considering these filters with poor out-of-band rejection performance, it can be seen that use of the MARCI filter set should easily allow the discrimination between oxidized  $\text{Fe}^{3+}$ -bearing minerals and unoxidized  $\text{Fe}^{2+}$ -bearing minerals, as well as the discrimination between anhydrous (hematite, maghemite) and hydrous (goethite, lepidocrocite)  $\text{Fe}^{3+}$ -bearing phases. Figure 6 is illustrative only, as we do not expect large deposits of such pure mineral phases to dominate the spectral properties of the Martian surface, even at the relatively high MA spatial resolution. A more realistic assessment of MARCI's performance comes from our simulations involving typical Mars bright and dark region telescopic spectra shown in Figure 7. As in Figure 6, all but MA4, MA6, MA7, and WA4 do an excellent job of reproducing the true spectral shape of these data. On the basis of previous telescopic and spacecraft remote-sensing studies, Martian spectral variability is known to be subtle, and most non-ice surface regions imaged by MARCI will appear similar

to these typical bright and dark region spectra or will have intermediate reflectivity but similar color. Thus it is encouraging that even despite limitations in spectral range, spectral sampling, and in some cases poor out-of-band rejection performance, the MARCI multispectral filters should be able to accurately quantify both color and albedo variability at an unprecedented spatial scale on Mars and relate this variability to true surface mineralogic and/or compositional differences.

### 3. Instrument Description

More details of the final MARCI design are given below and are summarized in the Table 1. Photographs of the final instruments are shown in Figure 8.

#### 3.1. Optics

**3.1.1. Foreoptics.** Two lenses are needed to cover the desired broad spectral range (225–800 nm) (Figure 9). The first covers the UV band only; it is a four-element  $f/7$  lens

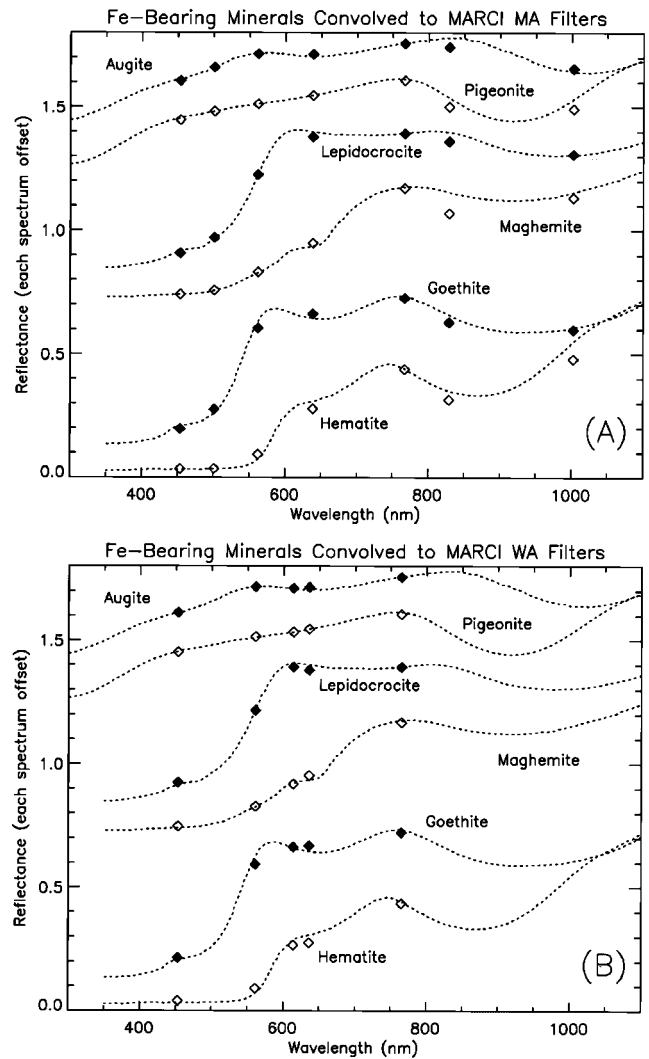


**Figure 6.** Results of convolving a set of pure  $\text{Fe}^{3+}$ -bearing and  $\text{Fe}^{2+}$ -bearing minerals over the MARCI filter band passes in Figure 5. Convolution method is described in the text. Laboratory data for augite and pigeonite are from *Clark et al.* [1993], and data for the iron oxides are from *Morris et al.* [1985].

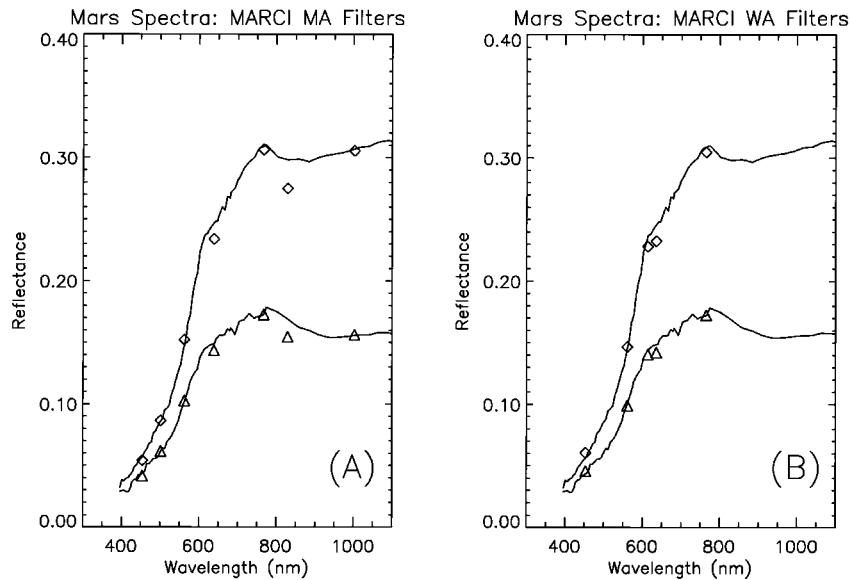


**Figure 7.** Results of convolving typical Mars bright and dark region telescopic spectra over the MARCI filter band passes in Figure 5. Convolution method is described in the text. Telescopic data are from *Mustard and Bell* [1994].

made entirely of fused silica. The lens is designed for optimal performance approximately halfway between the two UV wavelengths, and the modulation transfer function (MTF) degrades by a factor of  $\sim 3$  at the filter positions. The visible bands are imaged through a seven-element  $f/5$  lens made of optical glasses, all of which are qualified for space applications. The optical paths of the two lens systems are combined by a prism and dichroic beamsplitter so that all wavelengths are imaged onto the single focal plane array. The VIS bands are brought to the center of the array, while the UV bands are brought to one edge of the array. A baffle between the UV and visible (VIS) filters prevents cross-talk between their respective band passes. The UV system has a focal length of 4.69 mm; the VIS has a focal length of 4.27 mm. The field of view of the two systems is  $140^\circ$ . The WAC optics weigh  $\sim 120$  g.

The MA optics are more conventional when compared to the WA optics. They consist of an  $f/2$  catadioptric lens with an effective focal length of 87.9 mm. All surfaces are spherical, and there are six lens elements: five of  $\text{SiO}_2$  and one of BK7.

Owing to their very large FOV, the WA lenses would be extremely difficult to effectively baffle against stray light. As a result, they are not baffled and may occasionally experience performance degradation from stray light. The MA lens includes a 8.9 cm diameter, 5.3 cm high cylindrical baffle with 5 vane rings with a clear aperture of 5.4 cm.

**3.1.2. Filters.** The WAC uses four filter plates mounted directly over the area-array detector on the focal plane. Each plate consists of relatively narrow (50 nm) color filters, either singly or as adjacent strips. Each filter covers the entire cross-track width of the detector but only a fraction of the along-track portion of the detector. To acquire complete multicolor coverage, consecutive images are taken each time the instrument footprint advances by one filter's size in the downtrack direction. Band selection is accomplished by selectively reading out only part of the resulting frame for transmission to the spacecraft computer. We call this approach "push-frame" to distinguish it from the "push-broom" approach that uses line arrays.

The WAC VIS filter consists of 5 "stripes" each about 20 pixels in along-track extent. The entire detector is read out every 5.5 s. The five band passes were selected to provide good signal to noise and continuity with previous and ongoing color observations of Mars. The five bands selected were nominally intended to be centered at 425, 550, 600, 650, and 750 nm; the band passes are 50 nm (see Figure 5 and Table 2 for the actual band passes). To control out-of-band contributions, the two short-wavelength filters are deposited on Schott Glass BG-39, and the three longer wavelengths are deposited on Schott Glass OG-56. The filters were designed by and procured from Brysen Optical of Safety Harbor, Florida.

The WAC UV filters consist of two separate pieces, roughly  $10 \times 2$  mm, that mount near the edge of the detector. Both filters are deposited on fused silica substrates. The short-wavelength filter has a center wavelength of 280 nm, a band pass (full width at half maximum) of 69 nm, a peak transmission of 33%, and 23% transmission averaged over the passband. The longer-wavelength filter is centered at 315 nm, has a band pass of 17 nm, a peak transmission of 13%, and  $>10\%$  transmission averaged over the passband. The filters were designed by and procured from Barr Associates, Westford, Massachusetts.

Since the Kodak charge-coupled device (CCD) detector has little response in the UV, the detector side of the filter plate has been coated with Lumogen™, a UV-fluorescent material.

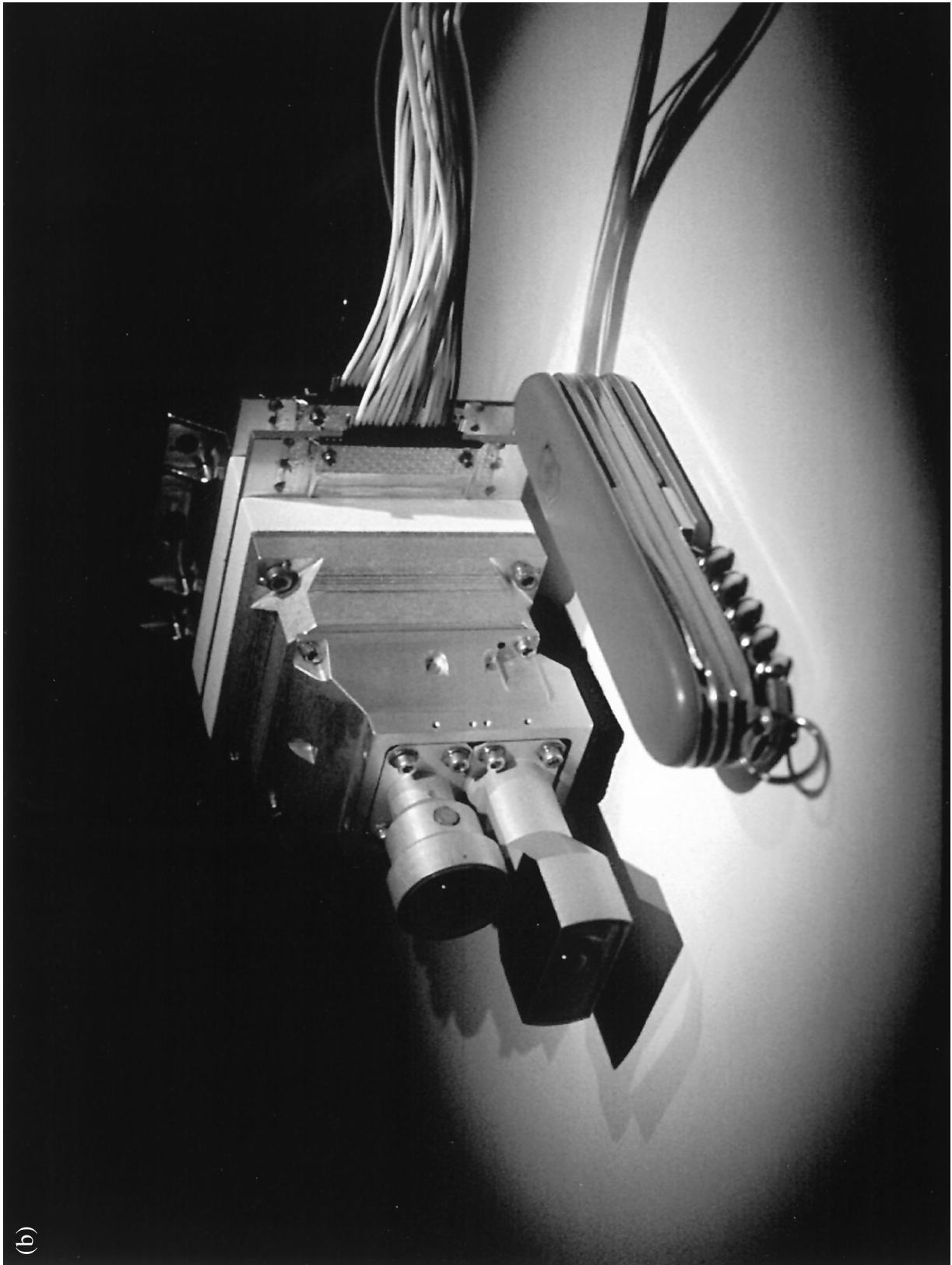
The MA camera uses eight "stripes," each  $\sim 100$  pixels in along-track extent. The entire detector is read out every 1.2 s. Table 2 lists the eight band passes and bandwidths. To control out-of-band contributions, the three short-wavelength filters are deposited on Schott Glass BG-39, and the five longer-wavelengths are deposited on Schott Glass OG-56. The filters were designed by and procured from Brysen Optical of Safety Harbor, Florida.

### 3.2. Electronics

The low-mass camera system developed by Malin Space Science Systems for the Mars Surveyor 1998 missions is a



**Figure 8.** Photographs of the Mars Surveyor 1998 Climate Orbiter (a) Medium Angle and (b) Wide Angle flight cameras. The pocket knife for scale is 8.9 cm (3.5 in) in length.



(b)

Figure 8. (continued).

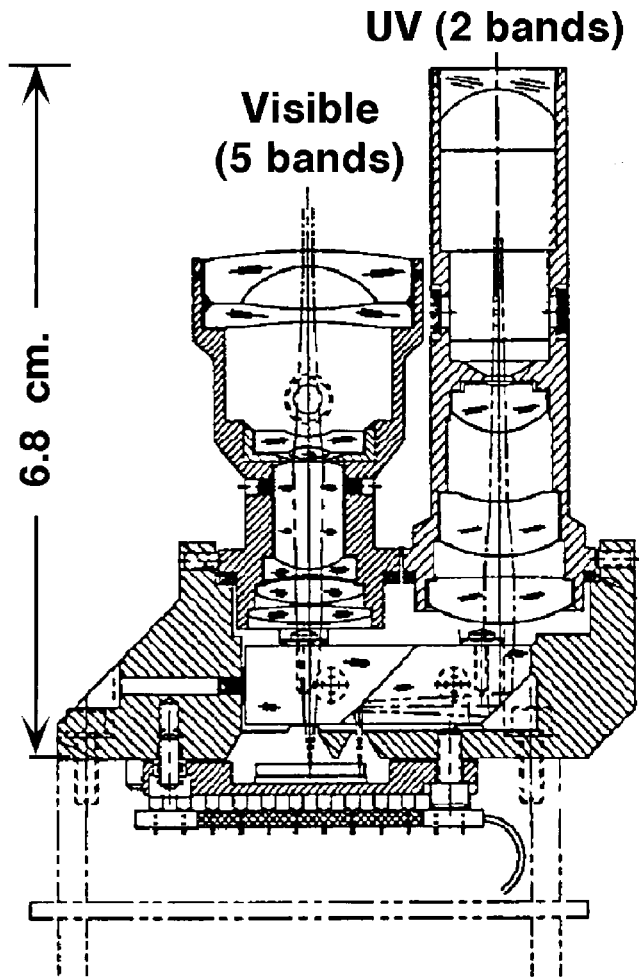


Figure 9. Full-scale drawing of WA camera optics.

logical development of previous designs for spaceborne CCD imaging systems. It uses the advances in sensor and computer technology realized in the 1990s to replace dedicated hardware with a flexible, software-driven design using a digital signal processor (DSP). A large electronically shuttered CCD with integral color filters replaces the complex filter wheel and mechanical shutter mechanisms of earlier systems. A block diagram of the electronics is shown in Figure 10.

**3.2.1. Detector.** The heart of the instrument is a Kodak KAI-1001 CCD. This detector has  $1024 \times 1024$  9-micron pixels ( $1018 \times 1008$  photoactive) and uses interline transfer to implement electronic shuttering. The KAI-1001's fill factor of 20% causes its quantum efficiency to be low, especially redward of 700 nm. These effects combine to make the detector comparatively poor in sensitivity, but the optics are sufficiently fast to compensate, allowing this compact CCD to be used.

Two capabilities of the detector can be used to reduce the raw data rate from the camera. First, on-chip summing can be used to add adjacent lines together in the charge domain under conditions of low signal. Second, the CCD's fast-dump feature can be used to read out only selected portions of the detector.

**3.2.2. Clock generation.** The CCD requires seven clock signals: a two-phase vertical clock (V1/V2), a two-phase horizontal clock (H1/H2), a substate clear clock (S), a reset clock (R), and a fast-dump clock (F). In addition, the analog-to-digital converter (ADC) requires a logic-level convert clock (C). The H1/H2 and R clocks are "fast" (maximum of  $\sim 3$  MHz), while the V1/V2, S, and F clocks are "slow" (maximum of  $\sim 20$  KHz).

The clocks are generated at logic levels by the DSP and are switched at the voltages required by the CCD using discrete P and N-MOSFET transistor pairs. There are two switch timing configurations: one for "fast" clocks, utilizing discrete HC-

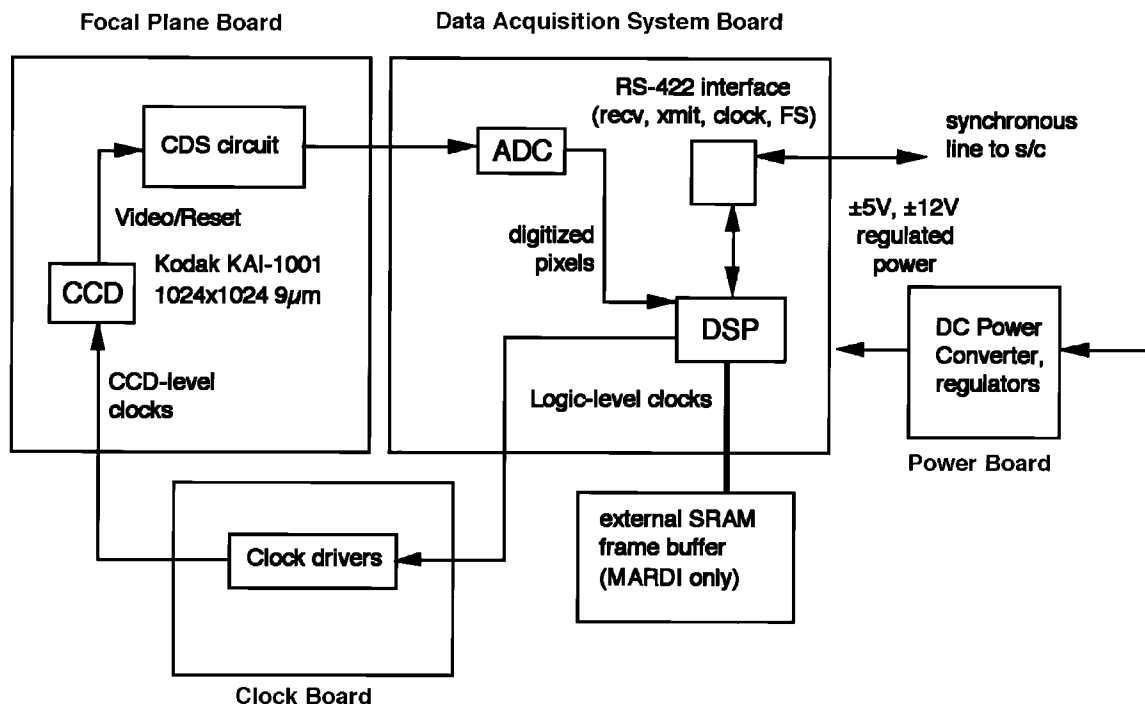


Figure 10. MARCI system block diagram.

family logic to synthesize fast one-shots, and one for “slow” clocks, which uses 74HC4538 integrated circuits (ICs).

**3.2.3. Analog signal processing.** The output signal from the CCD is alternating current (AC) coupled and then amplified by a single AD8011 opamp. To bring the amplified signal into the 0–5 V range accepted by the ADC, a fixed direct current (DC) offset is applied prior to amplification. The resulting AC-coupled signal encompasses half the ADC range: 1.25–3.75 V in the maximum signal condition of all pixels at full-well, and 0–2.5 V in the case where a small number of pixels are at full-well and the rest are near reset.

**3.2.4. Digitization.** The amplified CCD signal is digitized by an Analog Devices AD1672 12-bit ADC running at its maximum rate of 3 million samples per second (MSPS). For each pixel, both reset and video levels are digitized and then subtracted in the digital domain to perform correlated double sampling (CDS). Because of the dual sampling, the fastest pixel transfer time is 667 ns.

**3.2.5. System speed.** Maximum throughput is 667 ns per pixel, or about 0.75 s per full frame digitized. This speed limitation is a result of both the maximum digitization rate of the ADC and the maximum frequency of the analog clocks. The latter is in turn limited by the low-current voltage sources for the clock rails. Although higher rates could be achieved with this basic architecture by using higher-current (and hence higher-power) voltage sources and a faster (and hence higher-power) ADC, resource limitations dictated the present values.

**3.2.6. Digital electronics.** The digital electronics are responsible for clock pattern generation, sampling of the CCD signal, conversion of the 12-bit samples to 8-bit encoded pixels, storage of the pixels, and, finally, readout of the pixels to the spacecraft.

The DSP in the DAS permits full-speed software emulation of much of the usual analog processing, including CDS. Using software emulation, the zero reference (“reset”) level for each pixel is digitized and stored in a register. The sum of the video plus zero reference (“video”) level is then digitized, and an arithmetic subtraction is performed to produce the final result. The CCD output requires only scaling to the ADC range; no analog sampling, delay, or differencing is required.

The Motorola DSP56166 was selected because it can process 3 Mpixel/s (30 million instructions per seconds (MIPS)), it incorporates  $4\text{K} \times 16\text{-bit}$  data and  $2\text{K} \times 16\text{-bit}$  program memory on-chip, it has two  $\leq 15$  Mb/s serial ports that can be used simultaneously for a throughput of up to 30 Mb/s, and its firmware can be booted over these serial lines. For the nominal frame period of 0.75 s, it executes up to 20 arithmetic instructions per pixel. These performance characteristics enable the DSP to generate the CCD clocks, read the reset and video levels from the ADC, perform the correlated double-sampling subtraction, convert the pixel from 12 to 8 bits using a nonlinear transfer function, and apply lossless (2:1) first-difference Huffman compression and transmit it digitally with handshaking over the serial communication interface to the spacecraft CPU. The MARCI cameras operate using only the 8 K data static random access memory (SRAM) internal to the DSP.

The DSP clock rate at power-up is 10 MHz, supplied by the off-chip oscillator. This rate allows the fixed-rate 2 MHz serial data from the spacecraft to be loaded. Once active, the DSP runs at 60 MHz (30 MIPS) using its internal phase-locked loop. Lower-speed operation can be used to save power in standby and idle periods.

**3.2.7. Power supply and heater.** The instrument uses the Modular Devices MDI2690R-T15 power converter, which produces isolated +5 and  $\pm 15$  V from a nominal 28 V input. The ripple on the  $\pm 15$  V is excessive for the front-end video circuitry, so it is downregulated with series-pass regulators (LP2951 for +12 V and LM2990 for  $-12$  V) to remove ripple. The clock rail and DC bias voltages required by the CCD are generated by source-follower opamps and zener diodes and are appropriate to the current required.

Owing to a limitation on power switching imposed by the spacecraft, two Hewlett-Packard HSSR-7111 optocoupled solid-state relays are used internally to switch the +28 V input power between the electronics and the survival heater of each unit.

The survival heater is a 2-inch-square thin-film resistive heater fabricated by Tayco Engineering. It is mounted to the base of each unit and dissipates 3 W at the minimum spacecraft bus voltage of 22 V.

**3.2.8. Latchup protection.** The DSP is a commercial CMOS component with a low latchup threshold typical of such devices. To protect the DSP from damage that might be caused by radiation-induced latchup, a current-sense circuit on the power board senses increased latchup current and opens a crowbar transistor, shorting the +5 V output of the DC-DC converter to ground. This triggers the internal short-circuit protection of the converter, which removes power from the system for roughly 10 ms. The latchup reset is sensed by monitoring software in the spacecraft, which reboots the DSP appropriately. All other components are either adequately radiation-hardened or draw sufficiently low currents to be protected by current-limiting resistors.

**3.2.9. Health monitoring.** No dedicated internal instrument health monitoring is provided. Two temperature sensors (Analog Devices AD590) are provided, one on the FPA and one on the DAS board. These are monitored by the spacecraft computer. Instrument health diagnostics, including coarse measures of CCD voltage and temperature, are extracted from dark-current information.

**3.2.10. Form factor.** Both cameras consist of four circuit boards: the Focal Plane Assembly (FPA), the clock generation board (CLK), the Data Acquisition System (DAS), and the power regulation and switching board (PWR). The FPA is a five-layer rigid-flex polyimide-glass  $1.3 \times 1.3$  inch board whose rigid part is entirely contained within the instrument housing. The FPA flex cable passes through a slot in the housing and connects to the top of the CLK board.

The other three boards have an area for parts roughly 2.3 inches square. They are sandwiched between housing sections and are connected by flex cables on overhang regions outside of the housings. The DAS and CLK boards are 10-layer and six-layer, respectively, polyimide-aramid boards for thermal stability. The PWR board is a four-layer polyimide-glass board. All boards have parts on both sides.

In order to maintain a complete Faraday cage for interboard signals, the overhang region of each board is plated with a copper shield, except for a cutout for the flex cable pads. The flex cables are custom-fabricated with copper-mesh-plated Kapton layers on top and bottom and have shield traces on their outer edges conductively coupled to plated-through mounting holes. Once installed, copper-plated Kapton shields are placed over the connector pads on the board exteriors and conductively coupled to the circuit board copper shields. The boards are in direct conductive contact with the housing sec-

tions. Hence signals conducted between the boards via the flex cables are completely within the instrument's Faraday cage. The flex portion of the FPA is similarly shielded and connected.

This scheme was somewhat compromised for the spacecraft connectors, which are surface-mount types soldered directly to pads on the overhang regions of two of the circuit boards (DAS and PWR) on the side opposite to the interboard flex cables (conventional connectors with shells were not available in form factors that could fit in the constrained space). These connectors are 50-mil-pitch strip types whose pins are embedded in a Ryton matrix without metal shields. Metal tape is used to shield the connectors.

Radiation shielding is provided by aluminum housings with wall thicknesses of  $\sim 150$  mils. This reduces total dose to the 5–10 Krad(Si) level for the CLK, DAS, and PWR boards. Additional shielding is added to keep the FPA under 1 Krad(Si).

Electronics mass, including housings, is  $\sim 350$  g.

### 3.3. Software

Software runs on two processors: the main spacecraft central processing unit (CPU) and the DAS DSP. The CPU will be responsible for instrument operational commands and image postprocessing and compression. The DSP is responsible for generating the CCD clocks, emulating the required analog processing, and transmitting the data output to the CPU.

**3.3.1. DSP software.** The DSP software is written entirely in assembly language. As indicated previously, it performs all clock generation and pixel processing for the camera. Mission-specific versions of the software have been written to tailor the camera to the capabilities needed.

The MARCI code uses the internal SRAM space in the DSP for image storage. A double-line-buffer scheme allows one line to be read out to the spacecraft while a second is being captured from the CCD. This software also performs spectral band selection, editing, and summing. Summing can be performed either directly on pixel samples or, in cases where the signal is considerably less than the full-well, by accumulating multiple lines into the horizontal register before digitization.

**3.3.2. C&DH software.** MARCI cameras perform only minimal command and image processing internally. Using its serial communication line, each camera receives commands, operates upon them, and transmits the results to an external host processor. For the Mars Climate Orbiter spacecraft, that host processor is the spacecraft's main computer, the Command and Data Handler (C&DH). The C&DH is based on a 20 MHz RAD6000 processor board (a rad-hard derivative of the IBM/Motorola PowerPC architecture) built by Lockheed Martin Federal Systems Division.

Higher-level commanding, image processing, and fault protection are provided by instrument-supplied software running in the C&DH. The C&DH flight software is written in ANSI C for the VxWorks environment provided for the C&DH by Lockheed Martin Astronautics (LMA), the spacecraft manufacturer. It relies on LMA system services for basic functions such as uplink commanding, downlink data transfer, and communication with instrument hardware. The MARCI version of this code provides internal command sequencing for timed image acquisition and housekeeping functions, image memory allocation, communication with the camera hardware, and image processing. The latter includes additional pixel summing and editing and both lossless and lossy image data compression. The lossless mode uses a 2:1 Huffman first-difference

scheme; the lossy mode uses a discrete cosine transform operating on  $16 \times 16$  pixel blocks, requantization and zero truncation, and adaptive Huffman compression of remaining coefficients. This compressor was originally developed for the Mars Observer Camera flight software.

### 3.4. Interface

The MCO hardware interface is quite simple. The instrument is powered from an unregulated +28 V source. Two logic-level discrete lines (one for each camera) are provided to switch the power internally to the electronics and to the survival heater. Two temperature sensors per camera are provided for external monitoring of the electronics and focal plane. Each camera typically draws 3 W while imaging and  $< 2$  W while idle.

The serial communications interface uses RS-422 differential signaling to carry four signals. These four signals consist of a synchronous serial data transfer scheme common to Motorola, Texas Instruments, and Analog Devices DSPs; they are clock, frame sync, receive data, and transmit data. Only the transmit data is driven by the MARCI cameras (that is, the cameras are in "slave" mode). The maximum clock rate is 2.5 MHz for boot and 15 MHz thereafter. The clock runs continuously, and the frame sync is a 1-bit-wide pulse which signals the start of each 16-bit word or "frame." Although the interface allows full-duplex operation (data can flow both to and from the camera simultaneously), this capability is not typically used in practice, in part because of limitations in the C&DH serial interface implementation.

## 4. Mission Characteristics and Constraints

Mission characteristics, some imposed after selection, create constraints on the operation of and science return from the experiment.

### 4.1. Illumination Conditions

The original plan for Mars Surveyor 1998, described in NASA's Announcement of Opportunity (AO), was to place the orbiter in an early afternoon orbit (1300–1400 mean local solar time (MLST) at the equator). Such an orbit is nearly optimum for photometric and multispectral studies. After mission preliminary design the Mars Surveyor Project management elected to place the orbiter in a late afternoon orbit (1630–1700 MLST) in order to provide communications support to the 1998 lander. Mission design indicated that for the selected orbit, local solar time would oscillate by about an hour around a mean value and that with proper selection of orbit inclination, the mean value could be induced to vary monotonically. Thus it was theoretically possible to service the lander early in the mission and thereafter have the local time of the orbit migrate to lower incidence angles. Unfortunately, engineering decisions made subsequently to the Project decision compromised the spacecraft's ability to support low incidence angle observations (when solar eclipse durations exceed the spacecraft's power system capability). As a result, MARCI observations will mostly occur later than 1530 MLST, as shown in Figure 11.

### 4.2. Data Rates and Volumes

Figure 11 also shows the extremely variable data rates and volumes that will apply to the MCO, and in particular to MARCI. Data rates and volumes are initially low, primarily

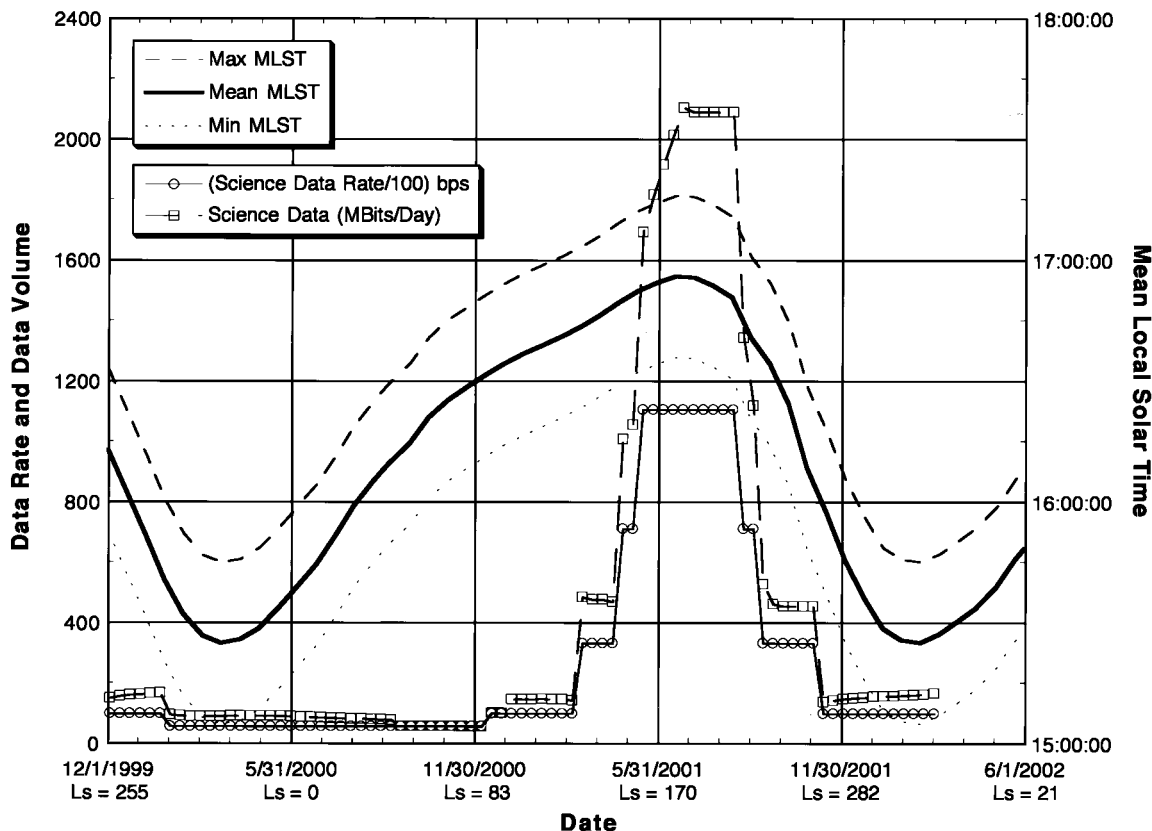


**Figure 11.** Data rates and mean local solar time as function of MCO mission duration. Data rates are very low throughout most of the mission, then peak in such a manner that over 80% of the data return occurs during a 7.5 month period. The late afternoon orbit was chosen to support lander operations at the beginning of the mission; it is decidedly not optimum for color imaging.

owing to the large Earth-Mars distances and secondarily to the allocation of data rate and volume to the Mars Polar Lander (MPL), for which the MCO acts as communications relay. After the MPL mission ends, data volumes decrease as the Earth-Mars range increases farther. Data rates and volumes begin to climb dramatically in March 2001, peaking in July before returning to the previous, low rates at the end of the mission (around January 2002). Over 80% of the camera's total data are returned during a 7 month period, and over 50% are returned during a 3 month period.

Three "representative" data return scenarios were examined

**Table 3.** Representative Imaging Capabilities as Function of Data Rate

Bands	Width	Sum- ming	Frame Time, ms	Rate, bps	Comment
<i>Representative MA Rate Required</i>					
1	1024	1	1.2	682,667	1 color, full resolution
2	1024	2	1.2	341,333	2 color, half resolution
5	1024	2	1.2	853,333	5 colors, 1/2 resolution
5	1024	3	1.2	379,259	5 colors, 1/3 resolution
10	1024	3	1.2	758,519	all colors, 1/3 resolution
<i>Representative WA Rate Required</i>					
1	1024	1	5	163,840	1 color, full resolution
7	1024	1	5	1,146,880	all colors, full resolution
7	1024	8	2.5	35,840	all colors, 1/8 resolution

by the Mars Surveyor 1998 Project during design of mission operations: Lander Relay, Aphelion (maximum Earth-Moon distance), and Maximum Data Rate.

During Lander Relay operations, most of the MCO down-link bandwidth is allocated to the MPL. Owing to the relatively small MARCI allocation (under 20 Mbits/d), a "typical" day's return might include global coverage in five of the seven WA color bands summed 11:1 (9.9 km/pixel) and compressed 5:1 using the lossy Mars Orbiter Camera MOC discrete cosine transform. It might also include about six MA images equivalent to 1 MByte each, also compressed 5:1. These images could be one  $40 \times 40$  km area covered in six color bands at 40 m/pixel, six  $40 \times 40$  km areas covered in one color band at 40 m/pixel, six  $40 \times 40$  km areas covered in four color bands at 80 m/pixel, or any of a variety of other resolution/coverage combinations. This mission phase lasts for  $\sim 90$  days.

When Mars is at aphelion, data return is power-limited. In this scenario, daily global WA coverage can expand slightly, but MA imaging is even more limited: all seven bands can be acquired, summed 9:1 (8 km/pixel), and compressed 5:1, but only about one third as much MA data can be acquired during this phase as can be acquired during Lander Relay operations. This mission phase lasts  $\sim 100$  days.

At the highest data rate, data virtually floods to Earth. For example, if the WA camera is operating continuously in all seven bands at 7 km/pixel compressed 5:1, observations equivalent to 373 MA images can be acquired, roughly 40% of which are compressed and recorded during noncommunication peri-

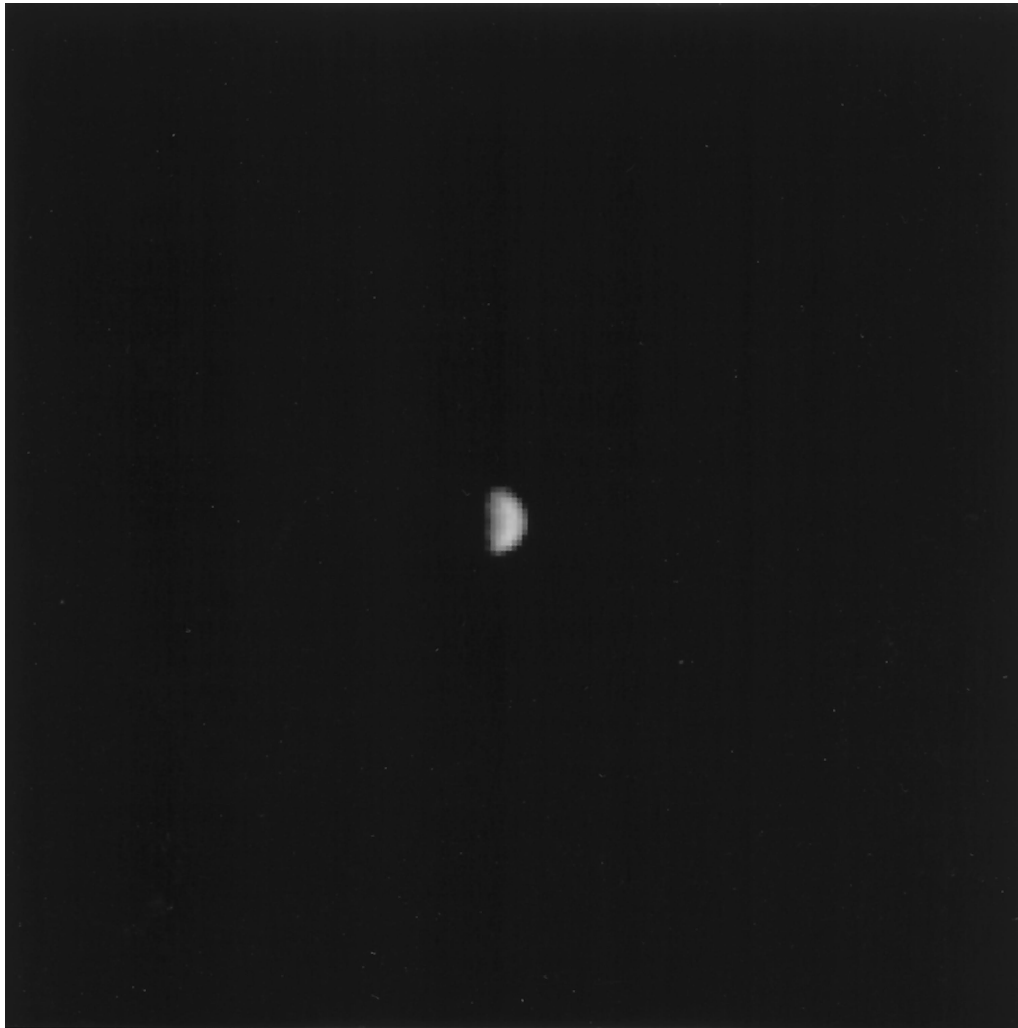


**Figure 12.** Approach image of Mars, the only science data returned from MCO. Mars is 15 pixels across.

ods and 60% of which are transmitted to Earth, uncompressed, in real time. Sustained for 3–4 months, such rates could permit 20% of the planet to be imaged at 40 m/pixel (or 80% at 80 m/pixel) in one color. During the 7 month high rate period, almost twice that amount of data can be collected; for example, it may be possible to image 70% of the planet at 80 m/pixel in two color bands. Trade-offs between resolution, areal, and color coverage are presently under consideration by the MARCI investigation team.

The data rate from the camera to the spacecraft imposes some constraints on imaging. Data transfer from the MARCI to the C&DH occurs at slightly over 1 Mbit/s. Table 3 shows some examples of instrument to C&DH bandwidth that meet the constraint. A typical combination might be five-band, 80 m/pixel MA and global WA images at 7 km/pixel, which would take ~900 Kbps.

## 5. Loss of Mars Climate Orbiter

The Mars Climate Orbiter was launched on December 11, 1998. Calibration observations of the Earth/Moon system, requested and authorized early in the development phase of the mission, were deleted by Project management decision just prior to launch. Later star calibrations demonstrated that the MARCI was fully functional and that it met the performance

specifications postlaunch and within the space environment. Owing to attitude control system vagrancies, only part of the planned star observations were successfully acquired. Imaging of Mars prior to orbit insertion was approved by the Project in midsummer 1999, although only at a distance from which the planet could barely be resolved (see Figure 12, acquired 18 days before arriving at Mars, when MCO was ~4.5 million km from Mars and the planet subtended 15 pixels). These were the first and only science data returned by the Mars Color Imager. The spacecraft and its science instruments were destroyed during the Mars Orbit Insertion maneuver, which occurred on September 23, 1999. The direct cause of the failure was a periapsis altitude too low in the atmosphere, the result of an error in navigation induced by the use of incorrect units on values related to forces acting on the spacecraft. The indirect causes of the failure, as described in the Mishap Review Board's report [*Stephenson et al.*, 1999], included poor training, insufficient personnel, and poor management decision-making processes.

**Acknowledgments.** The authors express their appreciation to the MARCI/MARDI hardware development team, led by M. Caplinger: Paul Otjens, Jeffrey Lewis, Jose Tamayo, Charles Schmitz, and Michael Ravine. We are extremely indebted to Steve Bailey for his efforts on our behalf during spacecraft assembly, test, and launch operations.

We thank Eldar Noe Dobrea for assistance with the MA and WA mineral deconvolution studies. MARCI was first conceived and developed under Planetary Instrument Definition and Development Program funding: the authors are indebted to William Quaide of NASA Headquarters (now retired) for his confidence in our effort and to T. Soulanille, K. Andrews, and T. Cushing (deceased) for the initial design study that eventually led to the MARCI. Optical Corporation of America designed and fabricated the two optical systems. This work was supported under JPL contract 960480.

## References

- Adams, J. B., Visible and near-infrared diffuse reflectance spectra of pyroxenes as applied to remote sensing of solid objects in the solar system, *J. Geophys. Res.*, **79**, 4829–4836, 1974.
- Barnes, J. R., J. B. Pollack, R. M. Haberle, C. B. Leovy, R. W. Zurek, H. Lee, and J. Schaeffer, Mars atmospheric dynamics as simulated by NASA Ames General Circulation Model 2: Transient baroclinic eddies, *J. Geophys. Res.*, **98**, 3125–3148, 1993.
- Barnes, J. R., R. M. Haberle, J. P. Pollack, H. Lee, and J. Schaeffer, Mars atmospheric dynamics as simulated by the NASA Ames GCM 3: Winter quasi-stationary eddies, *J. Geophys. Res.*, **101**, 12,753–12,776, 1996.
- Barth, C. A., C. W. Hord, A. I. Stewart, A. L. Lane, M. L. Dick, and G. P. Anderson, Mariner 9 ultraviolet spectrometer experiment: Seasonal variations of ozone on Mars, *Science*, **179**, 795–796, 1973.
- Bell, J. F., III, T. B. McCord, and P. D. Owensby, (1990) Observational Evidence of crystalline iron oxides on Mars, *J. Geophys. Res.*, **95**, 14,447–14,461, 1990.
- Bell, J. F., III, R. V. Morris, and J. B. Adams, Thermally altered palagonitic tephra: A spectral and process analog to the soils and dust of Mars, *J. Geophys. Res.*, **98**, 3373–3385, 1993.
- Bell, J. F., III, P. B. James, L. J. Martin, R. T. Clancy, and S. W. Lee, Mars surface mineralogy from Hubble Space Telescope multispectral imaging 1994 pre opposition data, *Proc. Lunar Planet. Sci. Conf. 26th*, 95–96, 1995.
- Bell, J. F., III, et al., Mineralogic and compositional properties of Martian soil and dust: Results from Mars Pathfinder, *J. Geophys. Res.*, **105**, 1721–1755, 2000.
- Blount, G., M. O. Smith, J. B. Adams, R. Greeley, and P. Christensen, Regional aeolian dynamics and sand mixing in the Gran Desierto: Evidence from Landsat and Thematic Mapper images, *J. Geophys. Res.*, **95**, 15,463–15,482, 1990.
- Calvin, W. M., and T. Z. Martin, Spatial variation in the seasonal south polar cap of Mars, *J. Geophys. Res.*, **99**, 21,143–21,152, 1994.
- Christensen, P. R., Martian dust mantling and surface composition: Interpretation of thermophysical properties, *J. Geophys. Res.*, **87**, 9985–9998, 1982.
- Christensen, P. R., Regional dust deposits on Mars: Physical properties, age, and history, *J. Geophys. Res.*, **91**, 3533–3545, 1986a.
- Christensen, P. R., The distribution of rocks on Mars, *Icarus*, **68**, 217–238, 1986b.
- Christensen, P. R., Global albedo variations on Mars: Implications for active aeolian transport, deposition, and erosion, *J. Geophys. Res.*, **93**, 7611–7624, 1988.
- Clancy, R. T., and S. W. Lee, A new look at dust and clouds in the Mars atmosphere: Analysis of emission-phase-function sequences from global Viking IRTM observations, *Icarus*, **93**, 135–158, 1991.
- Clancy, R. T., D. O. Muhleman, and G. L. Berge, Global changes in the 0–70 km thermal structure of the Mars atmosphere derived from 1975–1989 microwave CO spectra, *J. Geophys. Res.*, **95**, 14,543–14,554, 1990.
- Clancy, R. T., S. W. Lee, G. R. Gladstone, W. McMillan, and T. Roush, A new model for Mars atmospheric dust based upon analysis of ultraviolet through infrared observations from Mariner 9, Viking, and Phobos, *J. Geophys. Res.*, **100**, 5251–5263, 1995.
- Clancy, R. T., M. J. Wolff, and P. B. James, Minimal aerosol loading and global increases in atmospheric ozone during the 1996–97 Martian northern spring season, *Icarus*, **138**, 49–63, 1999.
- Clancy, R. T., A. W. Grossman, M. J. Wolff, P. B. James, D. J. Rudy, Y. N. Billawala, B. J. Sandor, S. W. Lee, and D. O. Muhleman, Water vapor saturation at low altitudes around Mars aphelion: A key to Mars climate?, *Icarus*, **122**, 36–62, 1996a.
- Clancy, R. T., M. J. Wolff, P. B. James, E. Smith, Y. N. Billawala, S. W. Lee, and M. Callan, Mars ozone measurements near the 1995 aphelion: HST ultraviolet spectroscopy with the FOS, *J. Geophys. Res.*, **101**, 12,777–12,783, 1996b.
- Clancy, R. T., B. J. Sandor, M. J. Wolff, P. R. Christensen, M. D. Smith, J. C. Pearl, B. J. Conrath, and R. J. Wilson, An intercomparison of ground-based millimeter, MGS TES, and Viking atmospheric temperature measurements: Seasonal and interannual variability of temperatures and dust loading in the global Mars atmosphere, *J. Geophys. Res.*, **105**, 9553–9571, 2000.
- Clark, B. C., A. K. Baird, R. J. Weldon, D. M. Tsusaki, L. Schnabel, and M. P. Candelaria, Chemical composition of Martian fines, *J. Geophys. Res.*, **87**, 10,059–10,067, 1982.
- Clark, R. N., G. A. Swayze, A. J. Gallagher, T. V. V. King, and W. M. Calvin, The U.S.G.S. Digital Spectral Library: Version 1: 0.2 to 3.0  $\mu\text{m}$ . *U.S. Geol. Surv. Open File Rep.*, 93-592, 1993.
- Cornell, R. M., and U. Schwertmann, *The Iron Oxides*, VCH, New York, 1996.
- Espenak, F., M. J. Mumma, T. Kostiuik, and D. Zipoy, Ground-based infrared measurements of the global distribution of ozone in the atmosphere of Mars, *Icarus*, **92**, 252–262, 1991.
- Geissler, P. E., R. B. Singer, G. Komatsu, S. Murchie, and J. Mustard, An unusual spectral unit in West Candor Chasma: Evidence for aqueous or hydrothermal alteration in the Martian canyons, *Icarus*, **106**, 380–391, 1993.
- Greeley, R., N. Lancaster, S. Lee, and P. Thomas, Martian aeolian processes, sediments, and features, in *Mars*, edited by H. Kieffer et al., pp. 730–766, Univ. of Ariz. Press, Tucson, 1992.
- Greeley, R. A., Skyeck, and J. Pollack, Martian aeolian features and deposits: Comparisons with general circulation model results, *J. Geophys. Res.*, **98**, 3183–3196, 1993.
- Haberle, R. M., and B. M. Jakosky, Atmospheric effects on the remote determination of thermal inertia on Mars, *Icarus*, **90**, 187–204, 1991.
- Herkenhoff, K. E., and B. C. Murray, Color and albedo of the south polar layered deposits on Mars, *J. Geophys. Res.*, **95**, 14,511–14,529, 1990.
- Herschel, W., On the remarkable appearances of the polar regions of the planet Mars, *Philos. Trans. R. Soc. London, Ser. A*, **24**, 233–273, 1784.
- Hollingsworth, J. L., R. M. Haberle, J. B. Pollack, A. F. C. Bridger, H. Lee, and J. Schaeffer, Winter storm zones on Mars, *Nature*, **380**, 413–416, 1995.
- Hord, C. W., K. D. Simmons, and L. K. McLaughlin, Mariner 9 ultraviolet spectrometer experiment: Pressure-altitude measurements on Mars, *Icarus*, **17**, 292–302, 1974.
- Jakosky, B. M., On the thermal properties of Martian fines, *Icarus*, **66**, 117–124, 1986.
- James, P. B., Martian local dust storms, in *Recent Advances in Planetary Meteorology*, edited by G. Hunt, pp. 85–100, Cambridge Univ. Press, New York, 1985.
- James, P. B., G. Briggs, J. Barnes, and A. Spruck, Seasonal recession of Mars' south polar cap as seen by Viking, *J. Geophys. Res.*, **84**, 2889–2922, 1979.
- James, P. B., H. H. Kieffer, and D. P. Paige, Seasonal cycle of CO<sub>2</sub> on Mars, in *Mars*, edited by H. Kieffer et al., pp. 934–968, Univ. of Ariz. Press, Tucson, 1992.
- James, P. B., R. T. Clancy, S. W. Lee, L. Martin, R. Kahn, R. Zurek, R. Singer, and E. Smith, Monitoring Mars with the Hubble Space Telescope: 1990–1991 observations, *Icarus*, **109**, 79–101, 1994.
- James, P. B., J. L. Hollingsworth, M. J. Wolff, and S. W. Lee, North polar dust storms in early spring on Mars, *Icarus*, **138**, 64–73, 1999.
- James, P. B., et al., The 1997 spring regression of the Martian south polar cap: Mars Orbiter Camera observations, *Icarus*, **144**, 410–419, 2000.
- Kahn, R. A., S. W. Lee, T. Z. Martin, and R. W. Zurek, The Martian dust cycle, in *Mars*, edited by H. Kieffer et al., pp. 1017–1053, Univ. of Ariz. Press, Tucson, 1992.
- Kieffer, H. H., T. Z. Martin, A. R. Peterfreund, B. M. Jakosky, E. D. Miner, and F. D. Palluconi, Thermal and albedo mapping of Mars during the Viking primary mission, *J. Geophys. Res.*, **82**, 4249–4295, 1977.
- Kieffer, H. H., K. F. Mullins, and T. N. Titus, TES pre-mapping-phase polar observations, *Eos Trans. AGU*, **79**(45), Fall Meet. Suppl., F533, 1998.
- Lee, S. W., P. C. Thomas, and J. Veverka, Wind streaks in Tharsis and Elysium: Implications for sediment transport by slope winds, *J. Geophys. Res.*, **87**, 10,025–10,041, 1982.
- Lee, S. W., R. T. Clancy, and T. Z. Martin, Spatial and temporal mapping of regional surface albedo and atmospheric dust opacity on Mars (abstract), *Bull. Am. Astron. Soc.*, **26**, 1112–1113, 1994.

- Magalhaes, J. A., and R. E. Young, Downslope windstorms in the lee of ridges on Mars, *Icarus*, *113*, 277–294, 1995.
- Martin, L. J., 1973 dust storm on Mars: Maps from hourly photographs, *Icarus*, *29*, 363–380, 1976.
- Martin, L. J., Clearing the Martian air: The troubled history of dust storms, *Icarus*, *57*, 317–321, 1984.
- McCord, T. B., R. N. Clark, and R. B. Singer, Mars: Near-infrared reflectance and spectra of surface regions and compositional implications, *J. Geophys. Res.*, *87*, 3021–3032, 1982a.
- McCord, T. B., R. B. Singer, B. R. Hawke, J. B. Adams, D. L. Evans, J. W. Head, P. J. Mougins-Mark, C. M. Pieters, R. L. Huguenin, and S. H. Zisk, Mars: Definition and characterization of global surface units with emphasis on composition, *J. Geophys. Res.*, *87*, 10,129–10,148, 1982b.
- McSween, H. Y., Jr., et al., Chemical, multispectral, and textural constraints on the composition and origin of rocks at the Mars Pathfinder landing site, *J. Geophys. Res.*, *104*, 8679–8715, 1999.
- Morris, R. V., H. V. Lauer Jr., C. A. Lawson, E. K. Gibson Jr., G. A. Nace, and P. J. Mougins-Mark, C. M. Pieters, R. L. Huguenin, and S. H. Zisk, Mars: Definition and characterization of global surface units with emphasis on composition, *J. Geophys. Res.*, *87*, 10,129–10,148, 1982b.
- Morris, R. V., D. G. Agresti, H. V. Lauer Jr., J. A. Newcomb, T. D. Shelfer, and A. V. Murali, Evidence for pigmentary hematite on Mars based on optical, magnetic, and Mössbauer studies of superparamagnetic (nanocrystalline) hematite, *J. Geophys. Res.*, *94*, 2760–2778, 1989.
- Morris, R. V., et al., Mineralogy, composition, and alteration of Mars Pathfinder rocks and soils: Evidence from multispectral, elemental, and magnetic data on terrestrial analogue, SNC meteorite, and Pathfinder samples, *J. Geophys. Res.*, *105*, 1757–1817, 2000.
- Mustard, J. F., and J. F. Bell III, New composite reflectance spectra of Mars from 0.4 to 3.14  $\mu\text{m}$ , *Geophys. Res. Lett.*, *21*, 353–356, 1994.
- Mustard, J. F., and J. M. Sunshine, Seeing through the dust: Martian crustal heterogeneity and links to the SNC meteorites, *Science*, *267*, 1623–1626, 1995.
- Mustard, J. F., S. Erard, J.-P. Bibring, J. W. Head, S. Hertz, Y. Langevin, C. M. Pieters, and C. J. Sotin, The surface of Syrtis Major: Composition of the volcanic substrate and mixing with altered dust and soil, *J. Geophys. Res.*, *98*, 3387–3400, 1993.
- Nair, H., M. Allen, A. D. Anbar, Y. L. Yung, and R. T. Clancy, A photochemical model of the Martian atmosphere, *Icarus*, *111*, 124–150, 1994.
- Ockert-Bell, M. E., J. F. Bell III, C. P. McKay, J. B. Pollack, and F. Forget, Absorption and scattering properties of the Martian atmospheric dust in the solar wavelengths, *J. Geophys. Res.*, *102*, 9039–9050, 1997.
- Pang, K., and J. M. Ajello, Complex refractive index of Martian dust: Wavelength dependence and composition, *Icarus*, *30*, 63–74, 1977.
- Peterfreund, A. R., Contemporary aeolian processes on Mars: Local dust storms. PhD dissertation, 246 pp., Ariz. State Univ., Tempe, 1985.
- Pollack, J. B., R. M. Haberle, H. Lee, and J. Schaeffer, Simulations of the general circulation of the Martian atmosphere, 1, Polar processes, *J. Geophys. Res.*, *95*, 1447–1474, 1990.
- Pollack, J. B., R. M. Haberle, J. R. Murphy, J. Schaeffer, and H. Lee, Simulation of general circulation of the Martian atmosphere, 2, Seasonal pressure variations, *J. Geophys. Res.*, *98*, 3149–3181, 1993.
- Ryan, J. A., and R. D. Lucich, Possible dust devils, vortices on Mars, *J. Geophys. Res.*, *88*, 11,005–11,011, 1983.
- Singer, R. B., and T. B. McCord, Mars: Large-scale mixing of bright and dark surface materials and implications for analysis of spectral reflectance, *Proc. Lunar Planet. Sci. Conf. 10th*, 1835–1848, 1979.
- Singer, R. B., T. B. McCord, R. N. Clark, J. B. Adams, and R. L. Huguenin, Mars surface composition from reflectance spectroscopy: A summary, *J. Geophys. Res.*, *84*, 8415–8426, 1979.
- Slipher, E. C., *The Photographic Story of Mars*, 168 pp., Northland, Flagstaff, Ariz., 1962.
- Soderblom, L. A., The composition and mineralogy of the Martian surface from spectroscopic observations: 0.3–50  $\mu\text{m}$ , in *Mars*, edited by H. Kieffer et al., pp. 557–593, Univ. of Ariz. Press, Tucson, 1992.
- Soderblom, L. A., K. Edwards, E. M. Eliason, E. M. Sanchez, and M. P. Charette, Global color variations of the Martian surface, *Icarus*, *34*, 446–464, 1978.
- Stephenson, A. G., D. R. Mulville, F. H. Bauer, G. A. Dukeman, P. Norvig, L. S. LaPiana, P. J. Rutledge, D. Folta, and R. Sackheim, Mars Climate Orbiter Mishap Investigation Board Phase I Report, 44 pp., NASA, Washington, D. C., Nov. 10, 1999.
- Stock, J., and A. D. Williams, *Astronomical Techniques*, edited by W. A. Hiltner, pp. 406–407, Univ. of Chicago Press, Chicago, Ill., 1962.
- Thomas, P. C., and P. J. Gierasch, Dust devils on Mars, *Science*, *230*, 175–177, 1985.
- Thomas, P. C., and P. J. Gierasch, Polar margin dunes and winds on Mars, *J. Geophys. Res.*, *100*, 5397–5406, 1995.
- Thomas, P. C., and C. Weitz, Sand dune materials and polar layered deposits on Mars, *Icarus*, *81*, 185–215, 1989.
- Thomas, P., J. Veverka, S. Lee, and A. Bloom, Classification of wind streaks on Mars, *Icarus*, *45*, 124–153, 1981.
- Thomas, P. C., S. Squyres, K. Herkenhoff, A. Howard, and B. Murray, Polar deposits of Mars, in *Mars*, edited by H. Kieffer et al., pp. 767–795, Univ. of Ariz. Press, Tucson, 1992.
- Thomas, P. C., et al., Bright dunes on Mars, *Nature*, *397*, 592–594, 1999.
- Veverka, J., P. Thomas, and R. Greeley, A study of variable features on Mars during the Viking primary mission, *J. Geophys. Res.*, *82*, 4167–4187, 1977.
- Wells, E. N., J. Veverka, and P. Thomas, Mars: Experimental study of albedo changes caused by dust fallout, *Icarus*, *58*, 331–338, 1984.
- Wolff, M. J., J. F. Bell III, P. B. James, R. T. Clancy, and S. W. Lee, Hubble Space Telescope observations of the Martian aphelion cloud belt prior to the Pathfinder Mission: Seasonal and interannual variations, *J. Geophys. Res.*, *104*, 9027–9041, 1999.
- Zurek, R. W., Martian great dust storms: An update, *Icarus*, *50*, 288–310, 1982.

J. F. Bell III and P. C. Thomas, Center for Radiophysics and Space Research, Cornell University, Ithaca, NY 14853.

W. Calvin, U.S. Geological Survey, 2255 North Gemini Road, Flagstaff, AZ 86001.

M. A. Caplinger and M. C. Malin, Malin Space Science Systems, P.O. Box 910148, San Diego, CA 92191-0148. (malin@msss.com)

R. T. Clancy, Space Science Institute, 1234 Innovation Drive, Suite 294, Boulder, CO 80303.

R. M. Haberle, NASA Ames Research Center, Space Sciences Division, MS 245-3, Moffett Field, CA 94035-1000.

P. B. James, Department of Astronomy, University of Toledo, Toledo, OH 43606.

S. W. Lee, Laboratory for Atmospheric and Space Physics, University of Colorado, Campus Box 392, Boulder, CO 80309-0392.

(Received July 13, 1999; revised February 11, 2000; accepted February 29, 2000.)